Size-Selective Transfer of Lipid Nanoparticle-Based Drug Carriers Across the Blood Brain Barrier Via Vascular Occlusions Following Traumatic Brain Injury

Igor Khalin, Nagappanpillai Adarsh, Martina Schifferer, Antonia Wehn, Bernhard Groschup, Thomas Misgeld, Andrey Klymchenko, Nikolaus Plesnila

To cite this version:

Igor Khalin, Nagappanpillai Adarsh, Martina Schifferer, Antonia Wehn, Bernhard Groschup, et al.. Size-Selective Transfer of Lipid Nanoparticle-Based Drug Carriers Across the Blood Brain Barrier Via Vascular Occlusions Following Traumatic Brain Injury. Small, 2022, 18 (18), pp.2200302. ⟨10.1002/smll.202200302⟩. ⟨hal-03872994⟩

HAL Id: hal-03872994
https://hal.science/hal-03872994v1

Submitted on 26 Nov 2022

Size-selective transfer of lipid nanoparticle-based drug carriers across the blood brain barrier via vascular occlusions following traumatic brain injury

Igor Khalin[1,2*], Nagappanpillai Adarsh[3,4], Martina Schifferer[2,5], Antonia Wehn[1], Bernhard Groschup[1], Thomas Misgeld[2,5,6], Andrey Klymchenko[3*], Nikolaus Plesnila[1,2*]

*Corresponding authors: igor.khalin@med.uni-muenchen.de; andrey.klymchenko@unistra.fr; nikolaus.plesnila@med.uni-muenchen.de

[1]Institute for Stroke and Dementia Research, University of Munich Medical Center, Munich, Germany; [2]Cluster for Systems Neurology, Munich, Germany; [3]Laboratory de Biophotonique et Pharmacologie, University of Strasbourg, Strasbourg, France; [4]Department of Polymer Chemistry, Government College Attingal, India; [5]German Center for Neurodegenerative Diseases, Munich, Germany; [6]Institute of Neuronal Cell Biology, School of Medicine, Technical University of Munich, Germany

The curren lack of understanding about how nanocarriers cross the blood-brain barrier (BBB) in the healthy and injured brain is hindering clinical translation of nanoscale brain-targeted drug-delivery systems. Here, we investigate the bio-distribution of lipid nano-emulsion droplets (LNDs) of two sizes (30- and 80-nm) in the mouse brain after traumatic brain injury (TBI). We prepared highly fluorescent LNDs by loading them with octadecyl rhodamine B and a bulky hydrophobic counter-ion, tetraphenylborate. Using *in vivo* 2-photon and confocal imaging, we studied the circulation kinetics and bio-distribution of LNDs in the healthy and injured mouse brain. We found that after TBI, LNDs of both sizes accumulated at vascular occlusions, where specifically 30-nm LNDs extravasated into the brain parenchyma and reached neurons. The vascular occlusions were not associated with bleedings, but instead surrounded by processes of activated microglia, suggesting a specific opening of the BBB. Finally, correlative light-electron microscopy revealed 30-nm LNDs in endothelial vesicles, while 80-nm particles remained in the vessel lumen, indicating size-selective vesicular transport across the BBB via vascular occlusions. As such, the vascular occlusions or microthrombi appeared to be a “gate” for nanocarriers through the BBB that open the exclusive new approach of brain targeting.

Key words: drug delivery; blood-brain barrier; brain injury; nanoparticles; correlative light-electron microscopy

INTRODUCTION

Traumatic brain injury (TBI) is the number one cause of death in young adults and children and characterized by acute and chronic neuroinflammation and axonal degeneration which result in severe cognitive, motor, and neuropsychiatric sequelae (1). Moreover, TBI increases the risk of neurodegenerative diseases, such as Alzheimer's or Parkinson's disease (2). To date, all clinical trials aimed to establish new pharmacological treatment for TBI have failed and thus no efficient therapeutic options exist to protect the brain from additional damage following a traumatic event (3).

A major hurdle for the development of novel pharmacotherapies for the treatment of central nervous system (CNS) disorders, including TBI, is the blood-brain barrier (BBB). The BBB bars many drugs from entering and accumulating in the brain parenchyma, therefore, BBB-permeable drug formulations often have to be applied in such high concentrations that the risk for adverse reactions is disproportionally elevated (4, 5). Therefore, there is an urgent need for the development of drug delivery systems which transport therapeutic molecules across the BBB and help to treat brain injuries.

Many studies have shown accumulation of nanoscale drug carriers in the CNS after TBI (6, 7) or the central effects of their cargoes (8, 9). For instance, we also previously demonstrated that brain-derived neurotrophic factor delivered by polymeric nanoparticles (NPs) accumulated in the injured mouse brain and improved neurological outcome (10), as well as, using real-time 2-photon microscopy, demonstrated the accumulation of ultrabright NPs around the lesion after stab brain injury (11). However, it still remains unclear how NPs are transported from the blood stream into the brain parenchyma - where this transport occurs - and which cellular elements are involved (12). Attempts to answer these questions were made by using magnetic resonance imaging and conventional fluorescence microscopy (6, 13). However, these approaches are so limited in resolution that many questions regarding the spatio-temporal dynamics of NPs in the healthy and injured brain still need to be answered (14).

To tackle this issue, our laboratories developed highly fluorescent NPs which could be visualized in the brain *in vivo* by using intravital two-photon microscopy, as well as other imaging modalities (11). Among different nanoparticles, lipid NPs are particularly attractive for biological applications due to their natural non-toxic lipid components (5). Lipid nanoparticles (NPs) recently showed a great promise of nanoscale drug-delivery systems when used for the delivery of mRNA-based COVID-19 vaccines (15). In addition to mRNA, lipid NPs are also able to carry small molecules or contrast agents and were recently considered to have great potential for CNS drug-delivery due to their lipid structure (16). In the current study, we aimed to investigate the applicability of lipid nano-emulsion droplets (LNDs) after TBI, which are characterized by their simple preparation, high loading capacity, biodegradability, excellent safety profile, and their great translational potential (17, 18). LNDs are composed of ingredients generally recognized as safe (GRAS) for the use in patients, such as natural oils and FDA-approved surfactants, thus having great potential in clinical translation. Moreover, it is known that lipid droplets can be visualized using electron microscopy (19). Highly hydrophobic fluorescent dyes can be efficiently loaded LNDs without their further leakage in biological media (DOI: 10.1039/c2ra21544f). Previous works showed that hydrophobicity of the cationic dyes and their brightness can be enhanced using bulky counterions, which enabled preparation of dye-loaded polymeric NPs (refs: 23, 24) and their application in vivo (refs 11,22 Khalin et al). The counterion approach was also successfully used for high loading of cyanine 3 dye into LNDs, which yielded bright fluorescent LNDs that can be tracked *in vivo* in zebrafish by multi-photon microscopy (11, 20-22). Moreover, using a FRET couple of near-infrared dyes with bulky counterions, it was shown that LNDs, despite liquid nature of their core, can preserve their integrity in the blood circulation for hours and enter xenografted tumours in nearly intact form (Ref. 20).

Here, we loaded LNDs with the fluorescence dye rhodamine coupled to a bulky counter-ion, which was expected to prevent aggregation-caused quenching of dyes and enhance dye loading. LNDs with a diameter of 30- and 80-nm were generated and used to track nanocarriers in the brain of living mice before and after TBI. Using *in vivo* imaging together with novel correlative light and electron microscopy (CLEM) techniques, we were able to unravel that LNDs cross the BBB in a size dependent manner in the penumbra of a traumatic brain contusion by endothelial transcytosis and at sites of microthrombus formation subsequently reaching spared neurons.

RESULTS

Formulation of LNDs

We formulated the fluorescent LNDs using the nano-emulsification approach (25), where oil, surfactant and dye are premixed together followed by addition of water. In this approach, the ratio of surfactant to oil can control the size of the obtained LNDs in a broad range of 20-150 nm. The rhodamine (R18), a fluorescent dye, was loaded into the LNDs because of its good two-photon absorption properties, high brightness and photo-stability (26). The counter-ion tetraphenylborate (TPB) was added to endow the cationic dye with higher hydrophobicity and thus enhance the encapsulation of rhodamine into the oil core of the LNDs (20, 21) and to minimize aggregation-induced quenching, thereby ensuring high single particle fluorescence (23, 27). By varying the oil/surfactant ratio, LNDs with hydrodynamic diameters of 33±3 and 85±4 nm (mean ± SD) as measured by dynamic light scattering (DLS), were prepared. LNDs loaded with 1 wt% R18/TBP with respect to oil had a fluorescence quantum yield of 17±2 %. The observed good quantum yield confirmed solubilisation of the dye in the oil core stabilized by the surfactant, without significant dye self-quenching. Considering the high number of loaded dye molecules per particle (84 and 1600 for 30- and 80-nm LNDs, respectively), the good quantum yield, the high extinction coefficient (125,000 $M^{-1}cm^{-1}$) and the two-photon absorption cross-section (200 GM) (26), both LNDs preparations are expected to have a high enough fluorescence intensity to be tracked by intravital multi-photon microscopy *in vivo*.

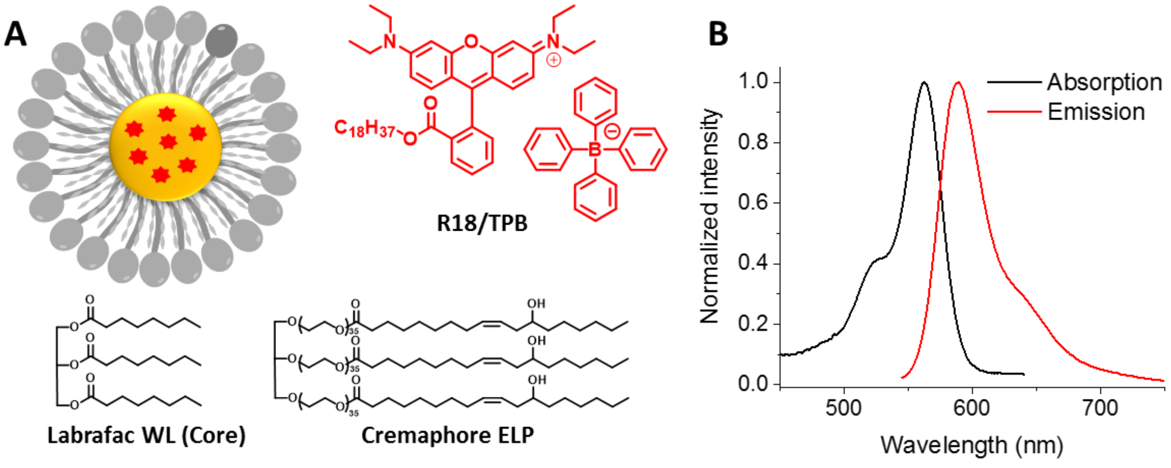

Figure 1. A. Schematic drawing of an LND consisting of the oil core (yellow; Labrafac WL), surfactant (grey; Cremaphore, Kolliphor® ELP), and the fluorescent dye rhodamine bound to a hydrophobic counter-ion (R18/TPB). **B.** Normalized absorption and emission spectra of 30-nm LNDs. The LNDs were diluted 500-fold in water. The final dye concentration was 2 µM.

In vivo imaging of LNDs in the cerebral circulation

30- or 80-nm LNDs were injected systemically via a femoral catheter in anesthetized mice and their distribution within the cerebral circulation was assessed for two hours by intravital two-photon microscopy (2PM) through an acute cranial window (**Figure 2A**). The fluorescent plasma marker fluorescein isothiocyanate (FITC) -dextran 2000 kDa was used to visualize cerebral vessels and served as a reference for vessel segmentation (**Figure 2B**; 0 min, FITC).

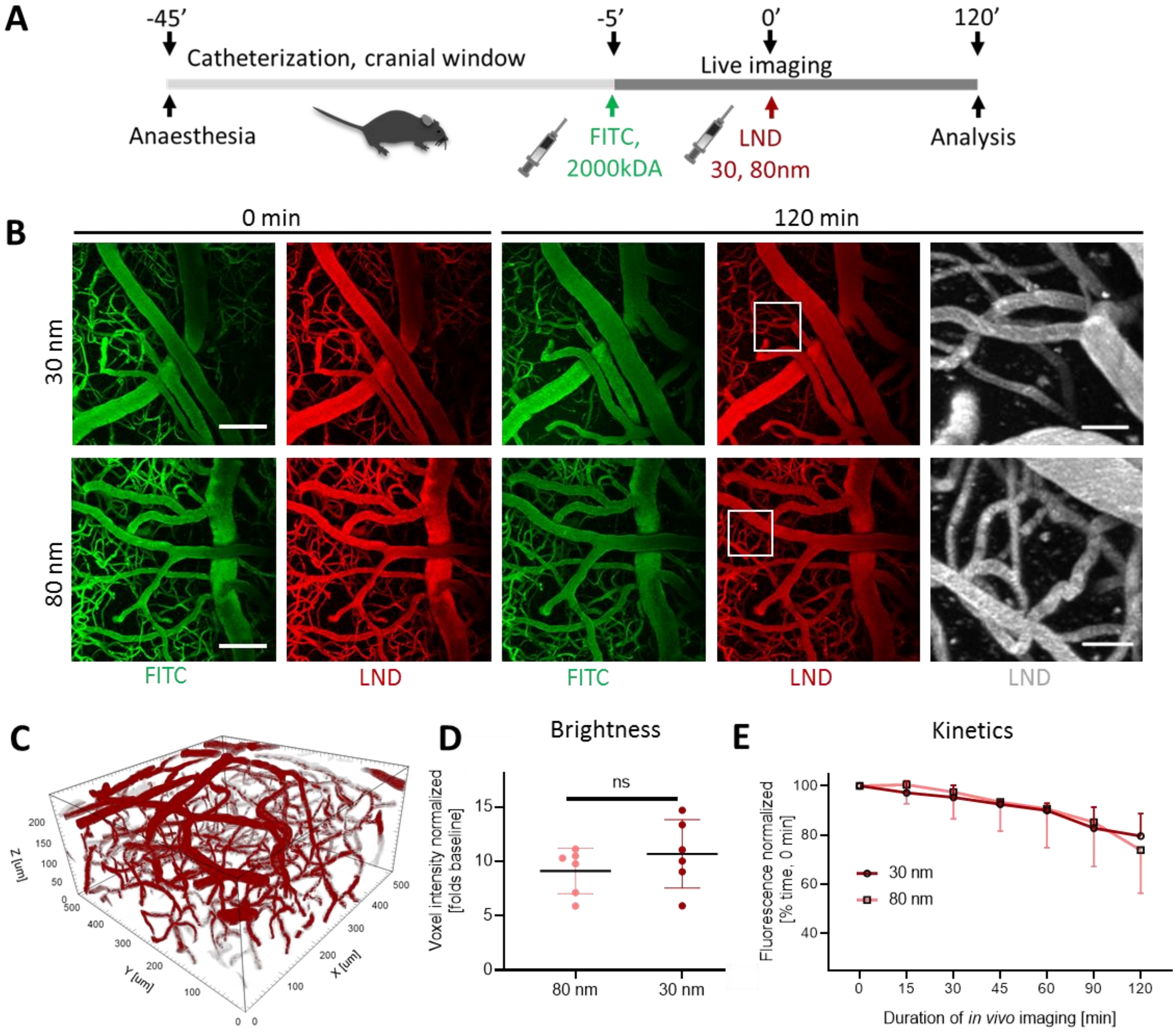

Figure 2. In vivo imaging of lipid nano-emulsion droplets (LND) in the cerebral circulation. A. Experimental design: surgical procedures (cranial window preparation, catheterization) and intravital imaging of injected LNDs. **B.** Maximum intensity projections of image Z-stacks recorded by 2-PM immediately after injection of LNDs and 120 min thereafter. Green - Fluorescein Isothiocyanate (FITC)-Dextran, 2000 kDA; red – LNDs 30-, 80-nm; grey – zoomed vasculature with LNDs. Z-stack, 250 µm depth, maximum intensity projection. Scale bar - 100 µm.

White outline – zoomed area of LNDs circulating in cerebral vessels. Scale bar - 20 µm. **C.** 3D view of LNDs circulating in cerebral vessels, processed with TubeAnalyst macros for FIJI software. **D.** 3D analysis of real-time brightness per voxel and **E.** Circulation kinetics of LNDs 30-nm vs. 80-nm, using TubeAnalyst. Data presented as means ± standard deviations. Statistical analysis: unpaired t-test (D) or two-way ANOVA (E) with Tukey correction for multiple comparison (n=6 for each group).

Shortly after injection, both 30- and 80-nm LNDs were observed in cerebral vessels (**Figure 2 B**; 0 min, LND). Within the observation time of two hours the LNDs of both sizes did not leave or occlude the lumen of any of the investigated vessel categories (pial arteries and veins, penetrating arterioles, cortical capillaries, or ascending veins; **Figure 2 B;** 120 min).

To analyse the brightness of the circulating LNDs over time at the voxel level we performed 3D segmentation of the vascular tree using a Fiji macro TubeAnalyst (IRB Barcelona) (28), in order to avoid artefacts of 2D projections **(Figure 2C**). The brightness of LNDs *in vivo* was independent of their size (**Figure 2D)** and remained relatively stable over time (**Figure 2E).** The brightness of the fluorescence signal of 80-nm LNDs two hours after injection was 73.9%±17.5 of the value determined immediately after injection (baseline). 30-nm LNDs showed a comparable stability (79.6%±9.1; p =0.94; two-way ANOVA; n=6). Since the decrease in circulated particle fluorescence was associated with the elimination rate of the LNDs from the systemic circulation (11), we were able to directly analyse the circulation kinetics of our LNDs. 30- and 80-nm LNDs had a circulation half-life more than 2 h, which was comparable with our previously published data (~ 4h) regarding circulation of cyanine loaded 80-nm LNDs in mice (20). This enables further collation of size-related LNDs' behaviour in mice with TBI.

Extravasation of LNDs in the mouse brain after TBI

Animals were subjected to TBI using a well-established mouse model (controlled-cortical impact; CCI) (29) and LNDs were injected systemically 60 min thereafter. This specific time point of particle injection was chosen since most TBI patients receive medical attention within the first hour after trauma. In order to investigate the biodistribution of LNDs in the cerebral vasculature and in the brain parenchyma, brains were perfusion fixed 30 or 120 min (**Figure 3A**) post-injection, removed, cut, and investigated by high resolution confocal microscopy.

First, we analysed the bio-distribution of 30- and 80-nm LNDs 90 min after TBI, *i.e.* 30 min after injection **(Figure 3A)**. Cascade Blue (CB) dextran (10,000 Da), a polysaccharide linked to a blue fluorescent molecule, which does not cross the BBB under physiological conditions, but is more than 10-fold smaller than LNDs, was injected along with LNDs to identify areas of the brain with a compromised BBB. Using this approach, we identified areas with a leaky BBB inside and around the cortical lesion, as well as in the hippocampus and the hypothalamus **(Figure 3B**; white arrows**)**. Using the red fluorescence channel to identify LNDs, we observed that deposition of LNDs of both sizes were co-localized with the areas of compromised BBB in the cortex and in the hippocampus **(Figure 3C,** white arrows, **and 3D)**, suggesting that LNDs specifically accumulated in injured tissue. Higher magnification imaging revealed by co-localization with lectin, that the majority of 30- and 80-nm LNDs accumulated within the lumen of cerebral microvessels **(Figure 3E**; white arrows**)**. Since LNDs did not accumulate spontaneously inside vessels (**Figure 2B**) and all non-adherent LNDs were removed from the circulation by perfusion fixation, the observed pattern of LNDs accumulation suggests that LNDs were incorporated into microvascular clots, so-called vascular occlusions

(VOs). So far, normally the formation of VOs after brain injury was observed by histology and in the pial microcirculation by *in vivo* microscopy (30), however, little to nothing is known about the kinetics of their formation and their role for the pathophysiology of TBI. Since LNDs seem to label VOs, discovery of LNDs' bio-distribution simultaneously elucidates spatial-temporal kinetics of VOs formation in the acute phase after TBI. Therefore, next, we investigated VOs density and the influence of LNDs size on VOs formation. To investigate a therapeutically relevant area, we focused on still perfused brain tissue surrounding the necrotic core of the contusion, the so-called traumatic penumbra (31). We defined the penumbra as the tissue labelled by lectin, *i.e.* the vascular dye injected minutes before sacrificing the animals, and having a compromised BBB as identified by CB extravasation **(Figure S1A**; yellow dashed line**)**. Using this approach, we calculated the volume of the traumatic penumbra to be around 2 mm^2 and to be the same in both investigated experimental groups (**Figure S1B**; p= 0.5662, unpaired t-test, n=9). Quantification within the traumatic penumbra showed that about 50 VOs were found per mm^2 and that the density of VOs was independent of the size of the injected LNDs **(Figure 3F**; p= 0.4682, unpaired t-test, n=9**).** Only very few VOs were observed outside the traumatic penumbra **(Figure 3D, E)** and here again the number of VOs was unrelated to LNDs size **(Figure S1C**; p= 0.9318, unpaired t-test, n=9**)**. Moreover, no VOs were found in non-traumatised tissue of the contralateral hemisphere. These results suggest that LNDs are trapped within VOs while they form and are therefore suited to label and target VOs.

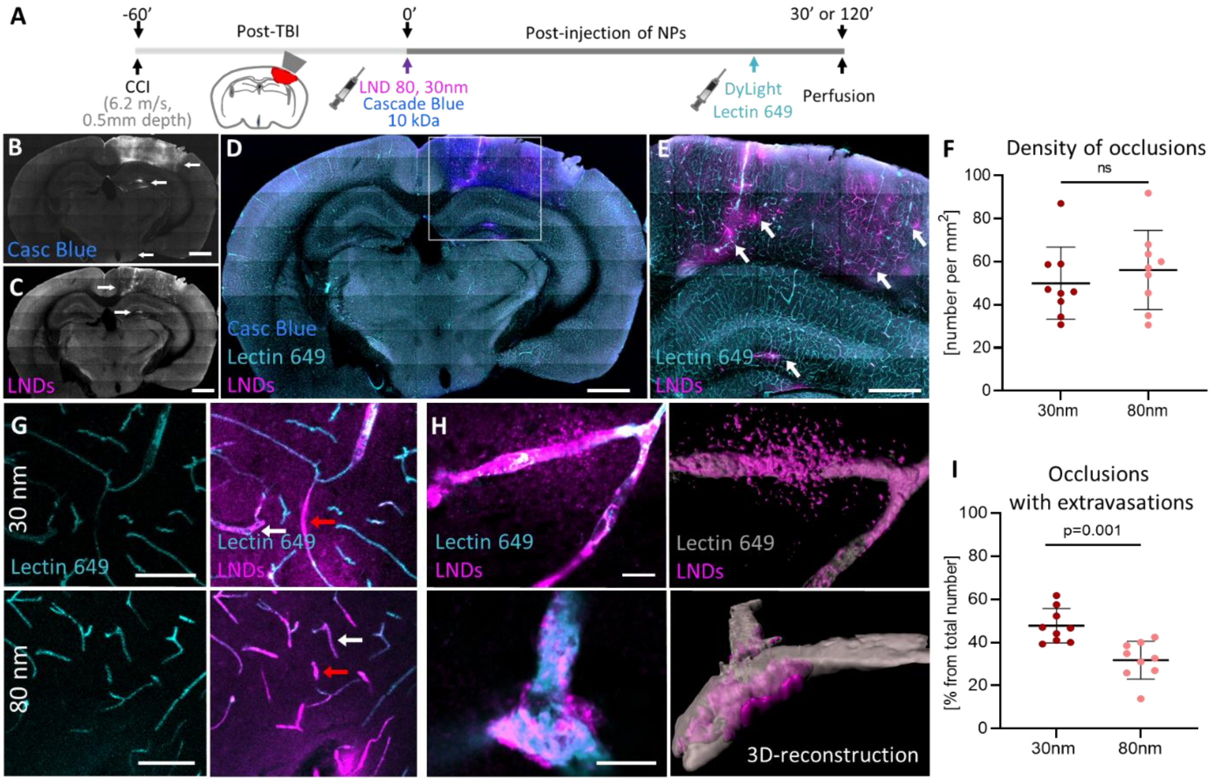

Figure 3. Lipid nano-emulsion droplets (LNDs) extravasate at sites of vascular occlusions following traumatic brain injury. **A.** Experimental design. CCI – controlled cortical impact; TBI – traumatic brain injury; LND – lipid nanodroplets. **B&C&D.** Coronal section of whole mouse injured brain 30 min after LNDs injection. **E.** Cortical lesion and hippocampus. Higher magnified area from D. White arrows: representative vascular occlusions (VO) with accumulated particles. 10x tile scan, maximum intensity projection of 60 µm z-stack. **F.** Quantification of the occlusions density in the lesion area. **G.** 30-nm and 80-nm NPs accumulated in VO of perilesional area. White arrow – vascular occlusions without extravasation; red arrows – with extravasation. **H.** Scanned z-stack of extravasation of LNDs through the occluded microvessel. Left panel – maximum intensity

projection; right panel – 3D-reconstruction. **G&H** – Upper panels: LNDs with 30-nm size, lower panels: LNDs with 80-nm size. Scale bars: B, C, D - 1 mm; E - 500 µm; G - 100 µm; H -10 µm. **I.** Quantification of the fraction of occlusions with extravasation. **F&I:** Data presented as mean ± standard deviation, 3 mice, 9 sections. Statistical analysis performed using GraphPrism®, unpaired t-test.

Interestingly, in some VOs LNDs, as was described above, remained inside the vessels **(Figure 3G**; white arrow**)**, whereas in others the particles expanded beyond the vascular lumen (lectin), which were identified as VOs with extravasation **(Figure 3G**; red arrow**)**. Using high resolution confocal imaging and 3D-reconstruction, we confirmed that in a number of VOs, large amount of LNDs were also localized outside the vessel lumen, *i.e.* within the brain parenchyma **(Figure 3H).** In general, 30-nm LNDs tended to extravasate more readily than 80-nm particles **(Figure 3H and Movie S1,2)**. Quantification of this process revealed that in mice injected with 30-nm LNDs, almost half of the VOs were accompanied by extravasation, which was 1.5-fold more frequent than in animals injected with 80-nm particles **(Figure 3I**; p= 0.001, unpaired t-test, n=9**)**. Since LNDs extravasated only at sites of VOs, this indicates a BBB semi-permeability at sites of VO formation which allows 30-nm LNDs to extravasate into the brain parenchyma. Hence, it is obvious that LNDs do not penetrate cerebral vessels by themselves, but need VOs to open the BBB for them first, as such LNDs extravasated into the brain originated from those initially accumulated inside VOs.

Next, we were interested to investigate the fate of LNDs which extravasated into the brain parenchyma. For this purpose, we used a similar experimental protocol as before, i.e. injection of LNDs after TBI, perfusion fixation and investigation of the traumatic penumbra, however, we allowed the particles to circulate for two hours **(Figure 3A)**. In order to define the area perfused by cerebral blood flow (CBF), animals were injected with fluorescent vessel labelling lectin some minutes before sacrificing **(Figure 3A)**. Confocal microscopy of full coronal sections revealed a lectin-positive "perfused" and a "non-perfused" area enabling to separate the lesion core from the penumbra **(Figure 4A)**. In the brain sections of both groups, VOs with extravasations were predominantly found perilesionally, close to the border between the penumbra and the lesion core **(Figure 4B**; white arrow**)**. Additionally, a substantial (fluorescence) signal in the LND channel from the extravasate inside the brain tissue surrounding the lesion core was also detected **(Figure 4B**; cyan arrow**)**, suggesting that after extravasation LNDs diffuse into the surrounding brain tissue. We analysed the average tissue penetration depth by LNDs from the lesion border **(Figure S2A)** and found that 30-nm LNDs diffused twice as deep into the brain parenchyma as 80-nm LNDs, i.e. 233±99 µm (mean±SD) **(Figure 4C**; p= 0.0007, unpaired t-test, n=15**)**. When quantifying how many LNDs were left inside the vessel lumen, we found significantly more 80-nm LNDs than 30-nm to be associated with intravascular clots **(Figure 4D**; p< 0.0001, unpaired t-test, n=146, n=341**)**, suggesting that more 30-nm LNDs extravasated into the brain parenchyma, while 80-nm preferentially stayed within the vessel lumen. The mean fluorescent intensity of the extravasate itself did not differ between 30- and 80-nm LNDs **(Figure S2B**; p= 0.3415, unpaired t-test, n=13, n=15**)**. Altogether, these results suggest, that 30-nm LNDs more readily leave the intravascular compartment at sites of VOs and, once extravasated, penetrate deeper into the brain parenchyma than 80-nm LNDs.

In order to identify whether extravasated LNDs interact with neuronal cells, we investigated the brain parenchyma at larger magnification. 30-nm LNDs diffused homogenously within the brain parenchyma **(Figure 4E**; upper row**)**, while 80-nm LNDs gathered around their site of extravasation **(Figure 4E**; lower row**)**. Extravasated 30-nm LNDs gathered in a fibre-like pattern with structures resembling synaptic boutons **(Figure 4E**; **i**, white arrows**)**, suggesting accumulation of 30-nm LNDs in neurites, *i.e.* axons and/or dendrites. Although some 80-nm LNDs also accumulated in neurites **(Figure S2C**; white arrow**)**, these larger LNDs were predominantly taken up by perivascular cells surrounding VOs **(Figure 4E ii**, white arrows**)**.

Interestingly, in non-perfused areas of the injured brain parenchyma, *i.e.* the core of the contusion, LNDs of both sizes were found within cells of different shape **(Figure S2C**; yellow arrows**)** which showed intense autofluorescence **(Figure S2C**; green arrows**)**. This suggests a random, non-specific accumulation of LNDs in dying cells.

Using intravital 2PM and the stab injury model **(Figure 3SA)**, we confirmed on alive animals that both sizes of injected LNDs accumulated inside VO, which surrounded the injury core **(Figure 3SB-D)**. We also confirmed that, 80-nm LNDs did not extravasate beyond the VO and neighboring cells **(Figure 3SE**; upper row**)**, while 30-nm LNDs diffused homogenously within the brain parenchyma **(Figure 3SE**; lower row**)**.

In order to verify the ability of LNDs to be taken up by and accumulate in neurons, we performed *in vitro* experiments. We exposed primary cultured rat neurons to LNDs **(Figure S4A)** and observed a gradual accumulation of NPs of both sizes in neurites already 30 minutes after incubation. The accumulation continued until the end of the observation time (120 min) **(Figure S4B, C, D).** Hence, these *in vitro* findings corroborate our *in vivo* data that LNDs, once extravasated, have a size-independent tropism towards neurons.

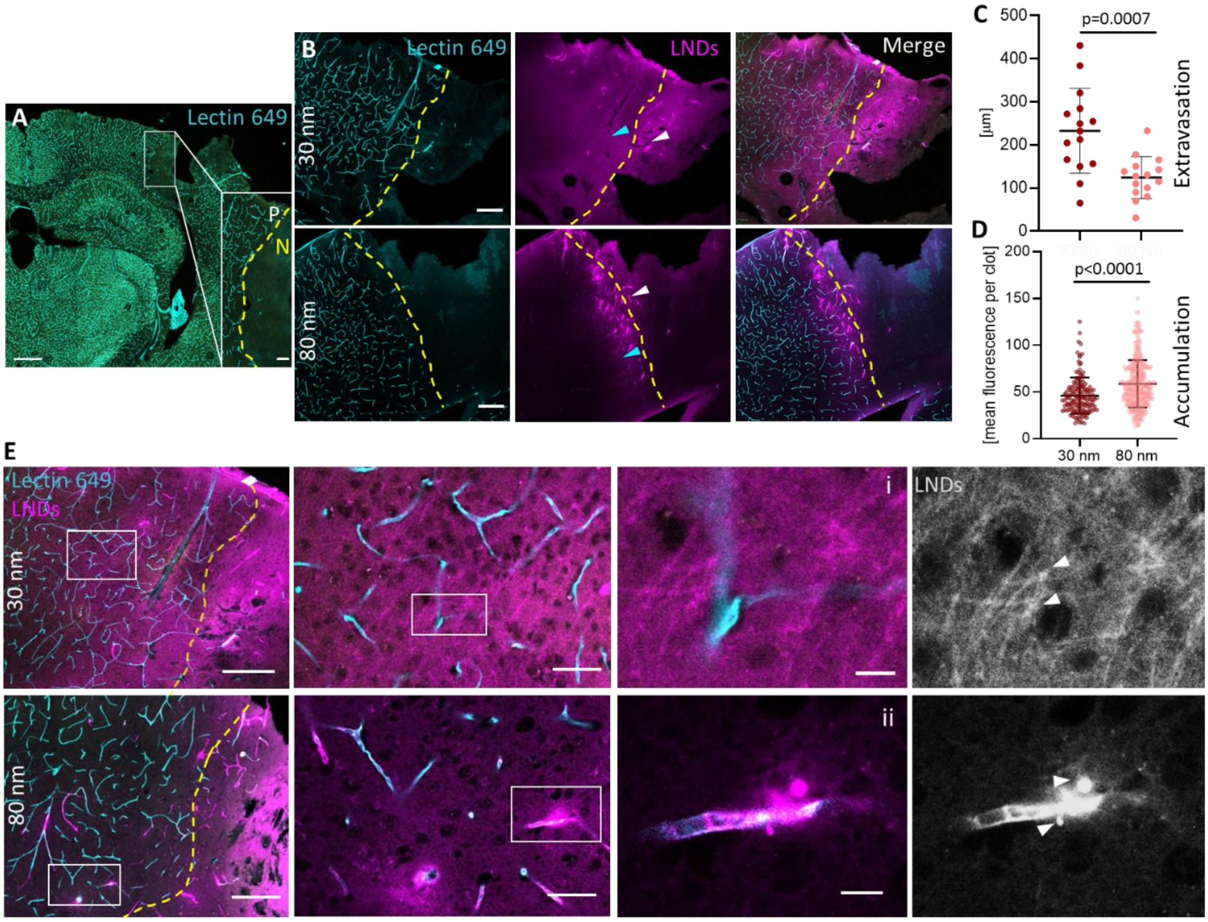

Figure 4. 120 min post-injection, 30-nm lipid nano-emulsion droplets (LNDs) diffuse deep into the brain parenchyma and are taken up by neurites. A. Representative coronal section of ipsilateral part of injured mouse brain. Lectin, injected shortly before perfusion, shows the perfused area. Zoomed insert: yellow dashed line – a virtual border between perfused (P) and non-perfused (N) areas. **B.** Extravasation of LNDs into perfused brain tissue 120 min after injection. Upper panel shows a representative image of mouse with brain injury injected with 30-nm LNDs; lower – 80-nm. White arrows – LNDs inside vascular occlusion (VO); cyan arrows – LNDs in brain tissue. **C.** Quantification of the depth of NPs diffusion into perfused tissue. Data presented as mean ± SD, 3 mice, 9 sections, 15 regions of interest. **D.** Quantification of the amount of accumulated NPs inside VO. Data presented as mean ± SD, 3 mice, 9 sections, 146 and 341 clots. Statistical analysis performed using GraphPrism®, unpaired t-test. **E.** Representative 40x magnification images of perfused brain area from the mouse injected with 30-nm NPs (upper panel) and 80-nm NPs (lower panel). Inserts – zoomed regions from perfused area. **i –** uptake of 30-nm LNDs by neuronal fibres. White arrows – structures suggestive axonal boutons. **ii** - uptake of 80-nm LNDs by cells surrounding the clots. White arrows – accumulation of particles inside structures suggestive endosomes. Scale bars: A – 500 µm, insert – 100 µm; B – 200 µm; E – 200 µm, insert – 50 µm; i, ii – 10 µm.

Mechanism of vascular permeability at sites of vascular occlusions.

In fact, the differential extravasation of smaller versus larger LNDs does not suggest disruption of cerebral microvessels, but rather an increase in vascular permeability. In order to exclude vascular disruption, we stained erythrocytes which are known to exit vessels only when the integrity of the vascular wall is completely compromised. To investigate the integrity of BBB, we co-stained microglia, which have recently been shown to react very early upon BBB opening (32). We again investigated the two-hour time point **(Figure 3A)**, but had to adjust our staining approach because LNDs turned out to be sensitive to the immunostaining protocol, *i.e.* the procedure destroyed the LNDs membrane and rendered them invisible due to a leakage of the incorporated fluorescent dye molecules. To solve this problem, we therefore performed a correlation between *in vivo* labelling and post-fixation immunostaining on the same brain slice **(Figure 5A)**. To do so, we first scanned the brain slice with injected lectin and LNDs by confocal microscopy, then performed immunohistochemistry and scanned the slice again. Using vessels as landmarks, we could then superimpose confocal images acquired from the same area for correlation. This enabled us to effectively stain the brain tissue while maintaining the full signal from the LNDs.

Applying this approach, we focused our analysis on VOs in the traumatic penumbra, since the lesion core contained only mechanically destroyed vessels **(Figure 5B, C)**. Within this area, we investigated ROIs containing VOs with extravasation **(Figure 5B, C** (*)**)**. Immunostaining with Ter119 revealed the absence of extravasated erythrocytes in the ROIs around the VOs, demonstrating that VOs in the traumatic penumbra are not associated with microbleeds **(Figure 5D)**. In contrast, stalls of erythrocytes were observed inside the lumen of VOs. Moreover, it was found that every single VO visualized by LNDs in the whole brain slice, was co-localized with erythrocyte stalls inside the vessels **(Figure 5D**; white arrows**)**, confirming that both 30- and 80-nm NPs accumulated inside microthrombi. Further, co-staining by Iba1 revealed that erythrocyte stalls were surrounded by microglial processes **(Figure 5E**; green arrows**)**. This morphological microglial phenotype was recently defined as microglia “rosettes”(32), an early marker (20-60 min) of BBB opening. We found such “rosettes” next to erythrocyte stalls throughout every single VO in the pericontusional area **(Figure 5F, G**; red arrows**)**, suggesting that every single VO is simultaneously the exact site of BBB opening and/or leakage. Morphological analysis of microglia surrounding VOs (vascular occlusion-associated microglia; VOM) demonstrated activation of these cells **(Figure S5)**, *i.e.* the circularity index of microglia significantly increased in the vicinity of VOs as compared to microglia, which was not associated with VOs (non-VOM) **(Figure 5H)**. VOM expanded their processes towards the VOs as indicated by the directionality index **(Figure 5I)**. The size of the particles did not play a role for this process. Furthermore, spatial correlative analysis of LNDs accumulated inside VOs, erythrocytes, and microglia by immunohistochemistry revealed 100% co-localization of VOs, erythrocyte stalls, the presence of activated VOM and particle accumulation/extravasation **(Figure 5J, K**; yellow arrows**)**. This, altogether, implicates that LNDs of both sizes are capable of being trapped in VOs between stalled blood cells and afterwards accumulated NPs start crossing the opened BBB in a size-dependent manner.

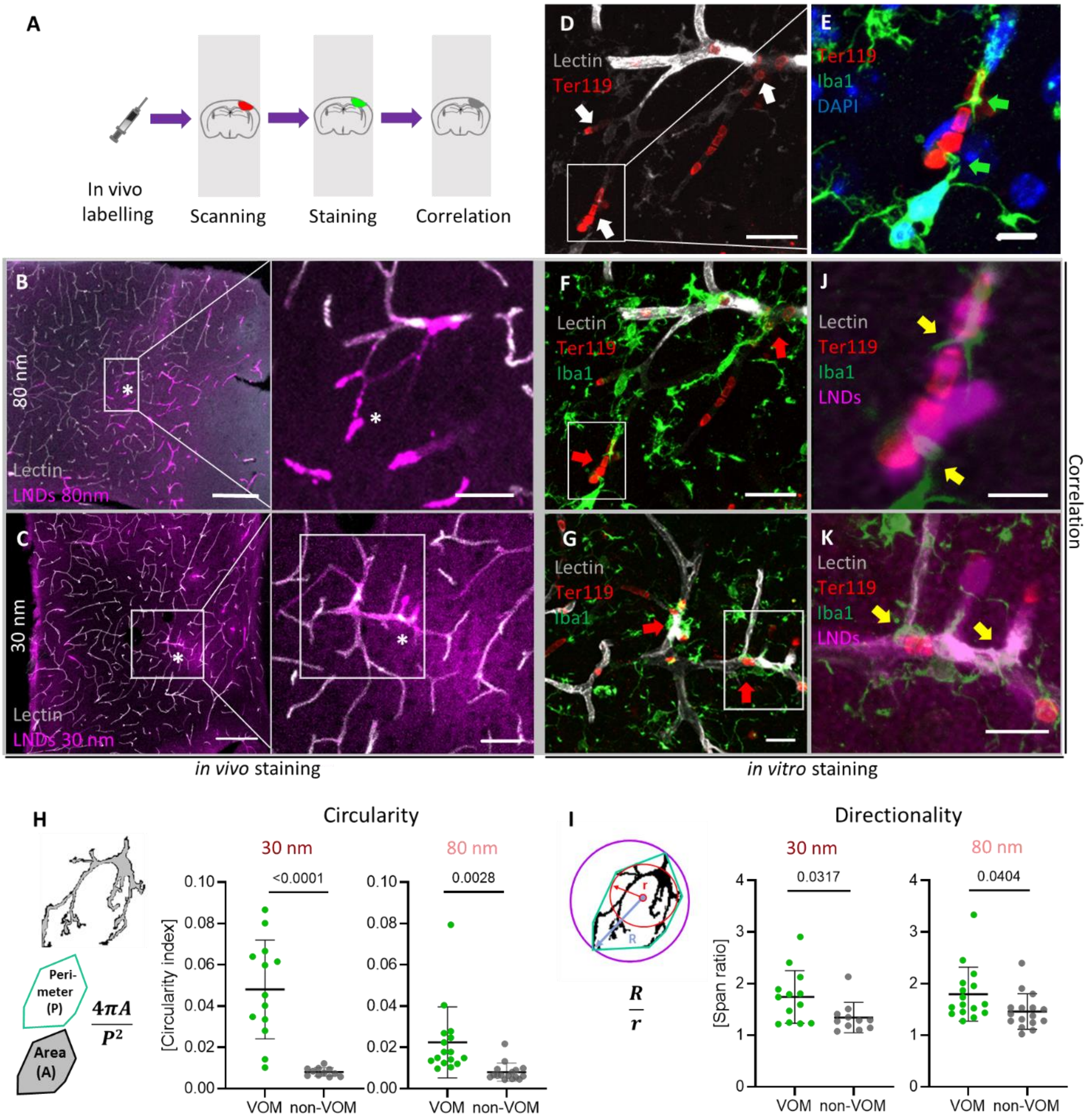

Figure 5. Vascular occlusion (VO)-induced extravasation of lipid nano-emulsion droplets (LNDs) is associated with activated microglia, but not with bleedings. A. The pipeline of correlation strategy of *in vivo* microscopy and post-fixed immunostainings. **B&C.** Representative confocal images of the cortical area of coronal sections of mice with TBI, 120 min post-injection with LNDs (magenta) 80-nm (B) or 30-nm (C). White rectangle – region of interest (ROI), containing VO with accumulated and extravasated LNDs, located in the pericontusional area. Scale bars: 200 µm; zoomed ROI – 50 µm**. D.** Matched ROI from B, stained with the erythrocyte marker Ter119 (red). Scale bar: 20 µm. White arrows indicate the sites of VO with LNDs accumulations. White rectangle: ROI containing VO. **E.** Zoomed VO, stained with Ter119, the microglia marker Iba1 and DAPI. Microglia processes - green arrows. Scale bar: 10 µm. **F&G.** Microglia processes surrounding VO with erythrocytes stalls (red arrows). Scale bar: 20 µm. **H&I.** Morphological analysis of microglia (circularity (H) and directionality (I)). VOM: VO-associated microglia; non-VOM: microglia are not associated with VO, cells far from the VO. Data presented as mean ± SD, n=15. Statistical analysis performed using GraphPrism®, unpaired t-test. **J&K.** Correlation of VO containing LNDs stained *in vivo* with *in vitro* post-fixed immunostaining shows that VO with accumulated LNDs contains erythrocyte stalls within vessel and microglia processes surrounding the vessel (yellow arrows). Scale bar: 10 µm.

Correlative light electron microscopy of vascular occlusions.

Next, we aimed to investigate the mechanisms by which LNDs extravasated at the site of VOs after TBI. For this purpose, we performed a similar experiment sacrificing the animal 2 hours post-injection (**Figure 3A)**, then we identified cerebral micro-vessels (lectin) and VOs (LNDs) by confocal fluorescence microscopy and investigated the surrounding cells and tissue by low- and high-resolution electron microscopy (EM) on the same vibratome section **(Figure 6A),** correlating the fluorescence signal with its ultrastructure.

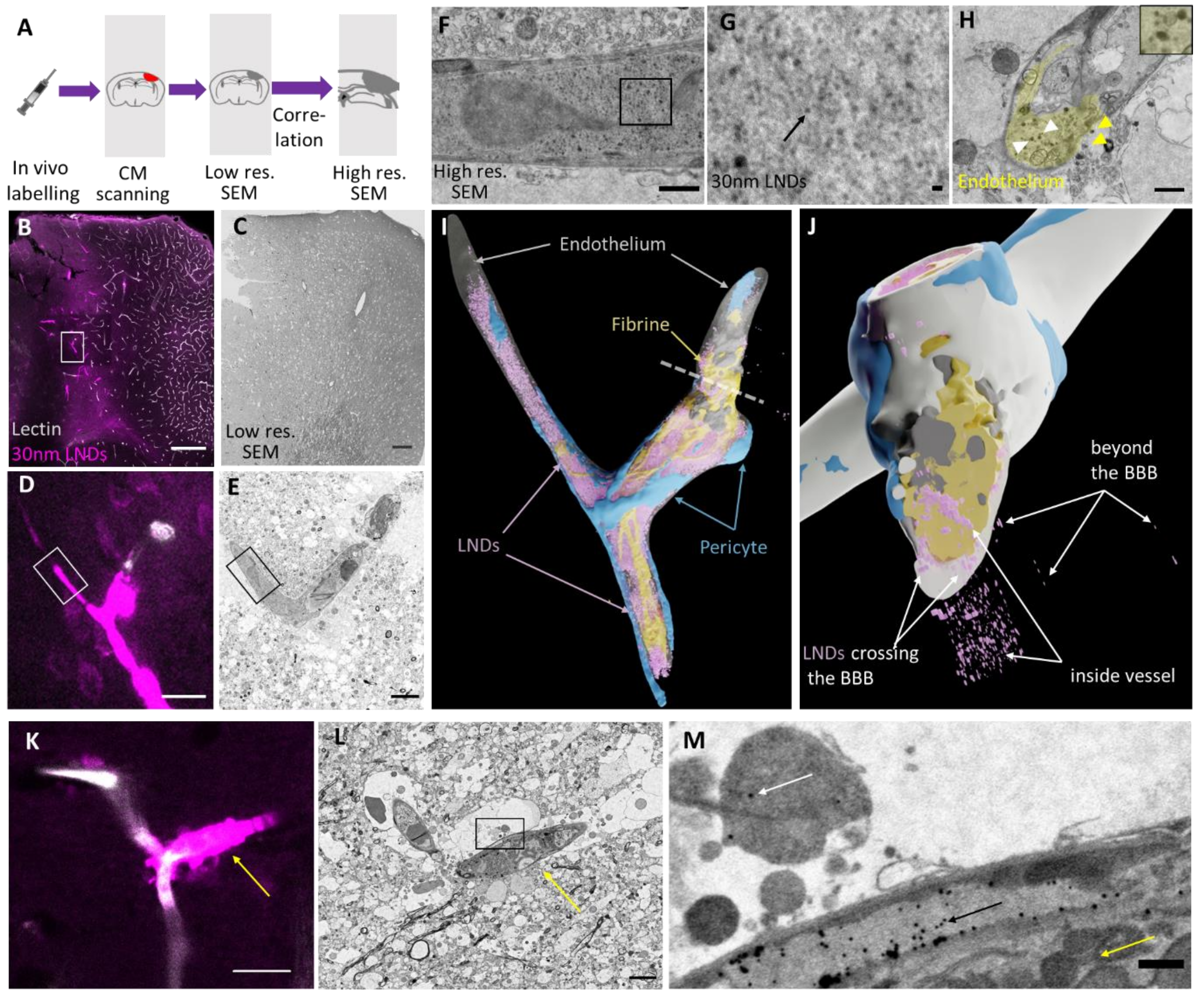

Figure 6. **Correlative light electron microscopy (CLEM) of lipid nano-emulsion droplets (LNDs) reveals extravasation of 30-nm particles through brain endothelial cell via vesicular transport. A.** The pipeline of correlation strategy of confocal microscopy and electron microscopy after *in vivo* labelling. CM – confocal microscopy; SEM – scanning electron microscopy; res. – resolution. **B.** Representative confocal image of the coronal cortical section of injured brain mouse, 120min post-injection of 30-nm LNDs (magenta), injected with DyLight Lectin (grey) minutes before sacrificing. Scale bar: 200 µm. **C.** Representative scanning electron microscopy (SEM) low resolution image of the pericontusional cortical area acquired on an ultrathin section of the same brain vibratome slice as in B. Scale bar: 100 µm; **D.** Region of interest (ROI), containing vascular occlusion (VO) with accumulated and extravasated LNDs, located pericontusionally. Insert from B. Scale bar: 20 µm**. E**. A higher resolution micrograph of ultrathin section correlated with D. Scale bar: - 5 µm. **F.** Representative high resolution SEM of vessels containing 30-nm LNDs. Scale bar: 2 µm; **G.** 30-nm LNDs (black arrow) inside VO. Zoomed ROI from F. Scale bar: 100 nm. **H**. 30-nm LNDs in the endothelial cytoplasm located inside vesicles (white arrow) and beyond the blood-brain barrier (BBB) in the brain parenchyma (yellow arrow). Scale bar: 1 µm. **I&J**. Rendered 3D-reconstruction of the ROI from D, E. LNDs (magenta), endothelium (grey), endothelial blebs (dark grey), pericyte (blue), fibrin (yellow). **K.** Representative confocal image of perilesional VO (yellow arrow) with accumulated/extravsated LNDs (magenta) co-injected with 30-nm gold nanoparticles. Scale bar: 20 µm. **L.** CLEM of VO from K. Scale bar: 5 µm. **M.** Trans-endothelial transport of gold nanoparticles (black arrow) at the site of VO (yellow arrow) beyond the BBB (white arrow). Scale bar: 500nm.

First of all, LNDs fluorescence of *in vivo* labelled traumatized mouse brain was conserved after supplementing the fixative containing glutaraldehyde, needed for optimal ultrastructural preservation **(Figure 6B)**. Accordingly, large confocal tile scans provided a map that allowed us to identify areas of the brain containing fluorescent LNDs accumulated inside VO together with structural landmarks (vessels labelled by lectin) which enabled the re-identification of the very same VO by high- and low-resolution EM (**Figure 6A)**.

The imaged brain subregion was subsequently dissected and processed for EM using a standard en bloc embedding protocol (33). We applied the ATUM (Automated Tape Collecting Ultramicrotomy) volume EM technique to serially ultrathin section and collect the entire thickness of the sample for subsequent volume scanning electron microscopy (SEM). Low resolution scanning (0.2 x 0.2 x 2 µm) was performed to cover the whole volume in order to screen for the ROI selected by light microscopy **(Figure 6 B&C)**. Using vessel patterns and section outlines as unique landmarks, the ROI from fluorescent microscopy was successfully re-located on the electron micrograph series **(Figure S6 A-D, E)** and selected for further high-resolution scanning **(Figure 6 D&E)**. SEM images obtained at different axial positions corresponded to the fluorescent signal from the acquired z-stack, reflecting a physical sectioning orientation, similar to the light microscopy focal planes **(Figure S6 F, G)**. This correlative light electron microscopy procedure was applied to brain tissue obtained from both 30- and 80-nm LNDs injected mice. As such, two high resolution SEM data sets of VOs were acquired – 30- and 80-nm, respectively **(Figure 6F, Figure S6 I)**. Surprisingly, individual LNDs inside VOs could be resolved by SEM **(Figure 6G, Figure S6 J)**. Ultrastructure-based size analysis showed that in mice injected with 30-nm the average diameter of the LNDs was 27.16 nm, while in mice injected with 80-nm – 62.21 nm **(Figure S6 K)**, indicating that non-damaged LNDs successfully reached the VOs after systemic injection. The slight difference between the mean particle diameter assessed by DLS (33±3 and 85±4 nm respectively) and SEM most likely originates from the fact that particles visualized by SEM were not always cut through their maximal diameter. Observing extravasations, 30-nm LNDs were, as expected, found to extravasate through the damaged basal membrane. However, surprisingly, they also were uptaken by vesicles in the cytoplasm of brain endothelial cells **(Figure 6H,** white arrows**)**, both individually and as aggregates **(Figure 6H**; insert**)**. Moreover, the particles were observed outside the non-damaged basal membrane **(Figure 6H,** yellow arrows**)**, suggesting trans-cellular vesicular transport. Based on these results, we performed a reconstruction of a VO with extravasated 30-nm LNDs to unravel their 3D-distribution **(Figure 6 I&J, Movie S3)** which confirmed 30-nm LNDs crossing the BBB via brain endothelial cells. In contrast, 80-nm LNDs were not found to penetrate through the non-damaged endothelium. Instead, they were accumulating inside the VOs, typically forming highly-density deposits **(Figure S6 L,** red arrows**)**. Looking around the VO, we found that 30-nm LNDs were internalized inside neurites in the perfused area **(Figure S6 H)** which represented healthy brain parenchyma **(Figure S6E**; black arrow**)**, as already suggested by light microscopy **(Figure 4E, i)**. However, near the border between non-perfused and perfused tissue, the LNDs were internalized non-specifically into the cytoplasm of degenerative cells **(Figure S6 M: i, ii)**, as was also observed above. Taken together, CLEM revealed that LNDs were capable to accumulate inside VO, but only 30-nm LNDs were taken-up by brain endothelial cell subsequently penetrating via transcytosis and reached neurites in non-injured pericontusional tissue. While the fluorescent LNDs were visible in the electron micrograph, we additionally probed trans-endothelial extravasation at the site of VO by co-injection of more discrete and electron-dense 30-nm gold NPs **(Figure S7 A)**. Using uniqueness of lesion borders and brain vasculature stained with lectin, we could again re-locate chosen VO containing fluorescent **LNDs (Figure 6 K&L; Figure S7 B-D**, white arrow, black rectangle**).** It was found using CLEM, that 30-nm gold NPs and LNDs successfully reached the VO **(Figure S7 E)** without any changes keeping their size and shape. Additionally, at the site of perilesional VO with extravasated fluorescent LNDs **(Figure 6 K,** yellow arrow**)**, 30-nm gold NPs were also transported beyond the BBB **(Figure 6 M,** black arrow**)** through non-damaged brain endothelial cell with intact tight junction **(Figure S7 G**, black arrow**)**, implicating trans-endothelial transport. Besides, using correlative immunostaining with a component of caveolae in cell membrane caveolin-1 (Cav-1) **(Figure S8 A,B)**, we found that vessel containing VO was highly expressing Cav-1 protein, while neighbouring non-affected vessels did not **(Figure S8 C,D)**. This altogether suggests that on the site of VO the BBB is losing its integrity and the increased permeabilization is associated with an activated caveolae-mediated transcytosis, which contributes to non-specific, but size-selective transcellular traffic of nanoscale drug carriers across the BBB.

DISCUSSION

TBI is the leading cause of death and disability in children and young adults worldwide, however, adequate treatments to prevent the development of post-traumatic neurodegeneration are still not available (3). Since targeted delivery of drugs into the healthy brain using nanomedicine is almost entirely inhibited by the BBB, understanding how acute brain injury influences the specific structural and functional characteristics of the BBB could reveal new opportunities for delivery of drugs in TBI (34). For example, many studies showed that the BBB opens acutely after brain trauma and NPs accumulate in the brain around the lesion after TBI (7, 35, 36), without demonstrating, however, any possible path or mechanism of particle penetration. Imaging modalities and complementing detecting technologies used did not allow to resolve where exactly NPs were biodistributed after the injury, as well as did not provide 3D visualization or dynamic changes. This shows that, unfortunately, the opportunity of BBB opening has not been fully exploited yet, and precise spatial and temporal opening of the BBB on the sub-cellular level and the interaction of nanoscale drug-delivery systems with the compromised cerebral microcirculation has not been discovered so far. Consequently, very little is known about the biodistribution of NPs in injured brain *in vivo*, and especially their dynamics. We think that exploiting new advanced imaging modalities and techniques able to provide 3D dynamic visualization of NPs biodistribution *in vivo* could enable the unraveling of this problem. Therefore, we developed novel, super-bright NPs, which can be visualized by 2-photon, confocal and electron microscopy, thus enabling to study *in vivo* BBB functional features related to brain-targeted drug-delivery.

Furthermore, *in vivo* measurement of permeability by direct imaging of fluorescent probes often includes dye leakage and dissociation of the probe from the fluorophore (37) leading to false positive results. In order to avoid this, we were using hydrophobic counterions for increasing of the hydrophobicity of the resulting rhodamine dye, thus improving encapsulation and substantially reducing the dye leakage (27). Additionally, the super-bright properties of NPs only unfold when the concentration of the rhodamine dye coupled with a tetraphenyl borate counter-ion is very high (38), therefore, the fluorescent signal from the leaked fluorophore will be reduced by several orders of magnitude and become undetectable. On the top of this, we exploited range of correlative imaging techniques preventing decomposition or flushing away the particles due to additional tissue processing. And finally, we additionally scanned autofluorescent channel, to control only true fluorescent signal from NPs. All these features, we hope, allowed us to provide accurate readouts avoiding unnecessary speculations. The advantages and potential of rhodamine/counterion-based organic NPs we already demonstrated in different *in vivo* microscopy modalities (11, 22), but have not yet been explored for LNDs. We chose lipid nanodroplets, since their simplicity in preparation and full biodegradability made them ideal as drug nanocarriers, which are composed of GRAS materials (17). Besides, lipid nanodroplets have already been proven stable and suitable for *in vivo* visualization when loaded with other bulky counterion-enhanced dyes (21).

We successfully visualized R18 loaded circulating particles *in vivo* using intravital 2-photon microscopy, thereby demonstrating that the clearance of both sizes LNDs was relatively slow. Long circulation time for LNDs was suggested by other studies, implicating also that their integrity in the blood circulation was not affected (20). These similar elimination rates specifically for respective sizes are in line with previous studies using pegylated gold nanoparticles (41). Considering these features and the similar voxel brightness of 30- and 80-nm LNDs we could unbiasedly further study particles' biodistribution dynamics in the traumatised brain.

Although many studies, including our previous works, already showed retention of NPs in the injured brain (11, 36) or brain-specific pharmacological effect of the cargo carried by NPs following the brain trauma (8, 10), the exact site of particle accumulation as well as the cellular and subcellular mechanisms of transfer could not be specified so far. Using super-bright LNDs and advanced imaging techniques, we first demonstrated that already 30 min after systemic injection, LNDs specifically accumulated in VOs around the brain lesion in penumbra. These post-TBI VOs, most likely caused by spontaneous intravascular microthrombi, were previously observed in the cortex and hippocampus of TBI patients by histology (42, 43) and in pial microvessels of mice after experimental TBI by *in vivo* imaging (44). The formation of VOs is known to be a dynamic process, which starts during the first hour after TBI and continues at least for 72 h. However, direct observation of VOs within the parenchymal cerebral microcirculation *in vivo* and the spatial-temporal changes of their formation have not been reported yet and represent one of the most interesting pathophysiological findings of the current study. Apparently, post-traumatic VOs contain platelets, fibrinogen and erythrocytes and are suggested to form in order to seal microendothelial leaks following TBI. At the same time, however, VOs may also contribute to further brain damage by causing or aggravating tissue ischemia (44-46). Our current results demonstrate that LNDs get trapped inside post-TBI VOs, thereby suggesting that, nanocarriers in general, and specifically 30-80-nm sized LNDs could be used to target VOs. Interestingly, other drug-delivery TBI studies investigated biodistribution of NPs which were commonly larger than 100 nm in diameter (6, 7, 40). It is likely that particles ended up inside VO, however, imaging techniques used did not allow to resolve particle distribution at a cellular level. Thus, showing for the first time that NPs accumulate inside VO after TBI, our data represents a novel approach to direct pharmacological substances to areas affected by microthrombosis.

Opening of the BBB for small molecules acutely and sub-acutely after TBI is well-documented both in humans and in preclinical animal models (47, 48), and typically results in the formation of brain edema. In line with these studies, we could demonstrate using fluorescent dextran CB that BBB opening occurs at cortical lesion, penumbra as well as hippocampus and hypothalamus 60-90 min post-CCI. It is known that extravasation of blood plasma occurs also in arterioles and venules, but mainly on the level of cerebral capillaries, as we could previously show by *in vivo* imaging (49). However, the undelaying cellular cause for the BBB leakage, also known as opening of BBB, remained unclear. In the current study, we demonstrated that following TBI, the opening of the BBB is not diffusely distributed, but occurs at the site of VOs. We found that 30-nm LNDs readily passed the BBB already 30 min after injection at place where VOs formed. At later time points, 30-nm LNDs reached the brain parenchyma and accumulated in healthy neurons, while the bigger 80-nm LNDs remained within or close to VOs. Since lesion core contains only non-functional and non-restorable damaged necrotic tissue, we focused our attention on the so-called penumbra, which is the area in-between healthy and necrotic tissue and therefore could potentially be treated therapeutically. Obviously, capillaries are dramatically damaged in lesion core and BBB simply is not existing and not able to stop bleedings or any blood components including LNDs of both sizes. Conversely, in penumbra VO-associated BBB permeability was not accompanied by bleeding, since red blood cells were always confined to the vessel lumen as well as never observed within the brain parenchyma. To identify why the BBB became leaky to structures below 80-nm only at the site of VOs, we hypothesized that VOs may, for instance, activate inflammatory cells, which in turn release inflammatory mediators, e.g. bradykinin (50, 51), which are known to increase vessel permeability. EM did not show any significant numbers of leukocytes within VOs, however, we found microglia surrounding VOs with increased permeability. VOs surrounded by activated microglia have recently been shown to occur at sites of increased BBB permeability after cerebral ischemia. Microglial activation was initiated by adenosine triphosphate released from astrocytes (32). Since VOs block the microcirculation, the area around the occlusion becomes hypoxic, thereby instantly inducing endothelial cell swelling as a very first reaction for this (52). Subsequently, these swollen endothelial cells become permeable to some blood-borne substances including circulated 30-nm LNDs. The presence of activated microglia as an indicator of opened BBB at VOs with absence of bleedings suggests that LNDs extravasation can occur through sites of non-ruptured endothelium in non-destroyed capillary. Thus, our results implicate both mechanistic insight of BBB opening after TBI and new phenomenon that VOs may serve as gates for the delivery of nanomedicines to the brain parenchyma.

Another important mechanistic question is how exactly LNDs cross the BBB. Detection of LNDs by CLEM enabled us to directly compare 30- and 80-nm LNDs inside and outside VOs and to identify their cellular and subcellular localization. When focusing on pericontusional tissue where tight junctions and endothelial cells are still intact, 30-nm NPs were found in endothelial vesicles, while 80-nm LNDs mainly remained inside VOs, i.e. in the vessel lumen. These data suggest that 30-nm LNPs as well as gold NPs are transported across the BBB via vesicular transport, thereby indicating a size-related limitation of endothelial vesicular transport at the BBB. These data are well in line with previous *in vitro* and *in vivo* reports that particles between 10- and 50-nm are more readily taken up by endothelial cells than larger NPs (41, 53, 54). Additionally, we showed that VOs in penumbra are associated with enhanced expression of Cav-1, a marker of membrane caveolae. It was shown before that particles of 30-nm size are known to be preferentially transported by caveolae-mediated uptake (55) and endothelial cell caveolae have a diameter of around 50-nm (56). Therefore, altogether our findings demonstrate that caveolar transport may play important role in trafficking of 30-nm LNDs across the BBB.

Taken together, our current data suggest the following mechanisms how LNDs cross the BBB after TBI: in areas of the traumatized brain where endothelial cells are damaged, LNDs of both sizes enter the brain parenchyma through the disrupted endothelial barrier. This scenario is mainly observed in the terminally damaged core of the traumatic contusion. In areas of the traumatized brain where the endothelium is still intact, i.e. the still salvageable pericontusional penumbral tissue, 30-nm NPs transcellularly cross the permeable BBB at VO site. Although the size of the transported NPs and high expression of Cav-1 at VO, suggest caveolar transport, further experiments are needed to identify the exact contribution of each molecular transport pathway, *i.e.* caveolin, clathrin, or non-specific cellular transport (5).

In addition to the mechanism of how LNDs cross the BBB after TBI, our current data also provide information about the fate of extravasated LNDs within the brain parenchyma in extracellular matrix ECM. While the few extravasated 80-nm LNDs stayed near their VO of origin and did not move significantly beyond the vessel wall, 30-nm particles penetrated much deeper into the brain parenchyma and reached neurons and neuronal processes. This finding is well in line with published data showing that the (ECM) of the brain parenchyma consist of channels with a diameter of 20-60 nm (57, 58). Thus, the diffusion of 80-nm LNDs was restricted by the pore size of the ECM, while 30-nm could easily diffuse along these channels and reach nearby neurons. Once reaching neurons, the uptake of LNDs was not size dependent as suggested by our *in vitro* experiments, where LNDs were directly applied to cultured neurons. Hence, not cellular uptake but the diameter of NPs is the main parameter responsible for the presence of LNDs in neurons after TBI. These data provide crucial information about future targeting strategies for CNS drugs: for targeting VOs or paravascular structures, NPs with a diameter of >80 nm should be used, while when also parenchymal structures are supposed to be targeted the applied NPs should not be larger than 30-nm. Although we do not have direct evidence whether the fully intact LNDs reached the neurons, the clear difference in quality and speed of extravasation in-between 30- and 80-nm LNDs additionally suggests that the detected signal originated mainly from NPs and not from leaked dye. Our earlier studies with forster resonance energy transfer-based LNDs showed that NPs can circulate non-destroyed for hours and enter vascularized tumour tissues in nearly intact form (20), which supports our conclusion. Nonetheless, acutely after TBI, during the crucial time while microthrombi are forming, the pharmacologically active compound loaded inside the 30-nm LND could be able to cure the microthrombi or protect the still viable neurons and potentially rescue them.

SUMMARY AND CONCLUSION

The overall mechanism of LNDs extravasation following the brain trauma is summarized in **Figure 7**. LNDs injected intravenously stay within healthy vessels and have a plasma half live of several hours **(Figure 7A)**. After TBI, 30- and 80-nm LNDs accumulate within VOs **(Figure 7B)**. In areas with a damaged BBB 30- and 80-nm LNDs extravasate into the brain parenchyma **(Figure 7C)**, while in areas with preserved BBB only 30-nm transverse the intact endothelium by vesicular transport **(Figure 7D)**. Once in the brain parenchyma, 30-nm LNDs diffuse over significant distances, reach nearby neurons and are taken up into their cytoplasm **(Figure 7E)**. The most important prerequisite for this process is that LNDs get trapped in VOs. Since the endothelial uptake of LNDs increases with decreasing velocity (59), it is comprehensive that a reduction of the velocity to zero within VOs greatly enhances the transport of LNDs across the damaged as well as the permeable BBB. Important to note, we are able to observe extravasation events only around VOs, probably because the amount of extravasating LNDs is dependent on their concentration at that site which is extraordinarily high at VOs due to LNDs accumulation. Possibly, the extravascular LNDs signal at other places of extravasation is below the detection limit of confocal microscopy, but, therefore, the number of extravasated particles there is also negligible.

The postulated mechanism **(Figure 7)** also sheds light on the so-called enhanced permeability-retention effect (EPR), previously used to explain how NPs reach the brain following the brain trauma (60) and could therefore deepen the understanding of nanoscale drug-delivery system extravasation in other types of acute brain injury or diseases associated with microthrombosis. However, the latter would need additional experiments.

Taken together, our current data unravel the tissue, cellular and subcellular mechanism by which LNDs cross the BBB after TBI thereby paving the way for new application of LNDs as drug carriers for the treatment of the injured brain.

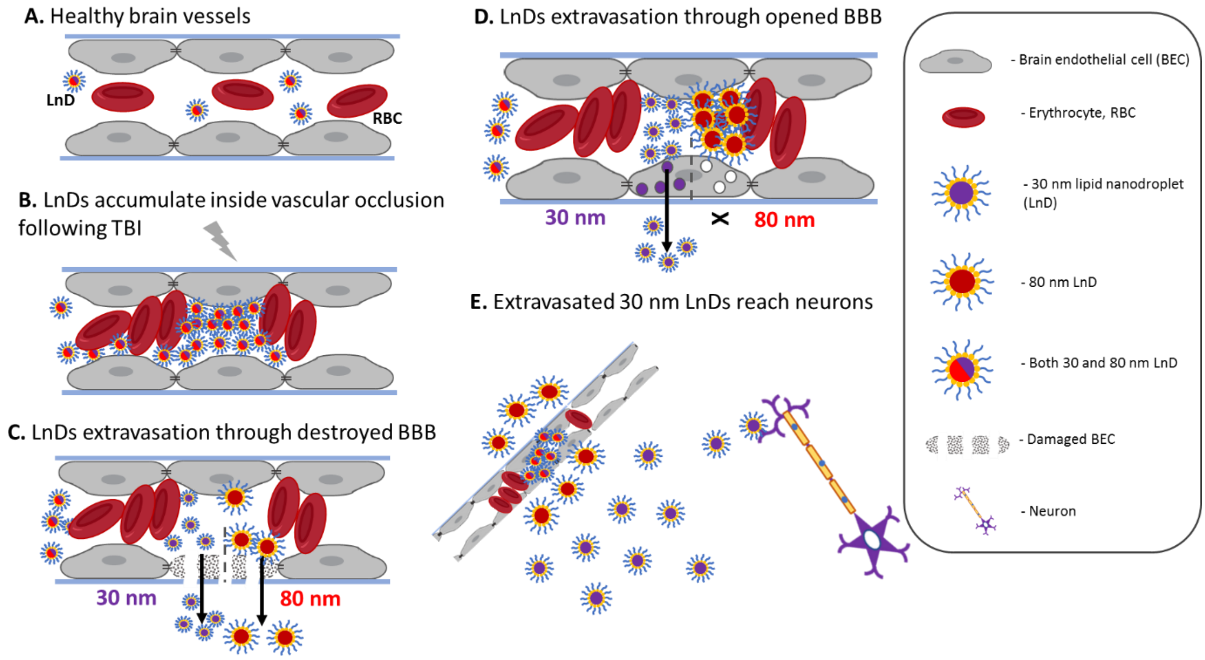

Figure 7. Mechanism (stages) of nanoparticles extravasation in penumbra through vascular occlusion following brain injury. 1. Circulation of both 30- and 80-nm lipid nanodroplets in healthy vessel and with closed blood-brain barrier (BBB). 2**.** Formation of vascular occlusion (microthrombus) following the traumatic brain injury (TBI) provokes accumulation of LNDs between the trapped cells. **3.** 30-nm, but not 80-nm LNDs accumulated inside vascular occlusions are extravasating via intracellular vesicles of swollen endothelial cell (BBB is open). **4.** Both 30-nm and 80-nm LNDs are extravasating through damaged brain endothelial cell (BBB is destroyed). **5.** 80-nm LNDs, predominantly, stay around the vascular occlusion, while 30-nm LNDs reach the neurons in healthy areas.

MATERIALS AND METHODS

Lipid nanodroplets

Dye loaded lipid nanoemulsions droplets were produced by spontaneous nanoemulsification by adapting previously described protocols (20). Briefly, the dye R18/TPB (prepared as described earlier (23)) was firstly dissolved in LabrafacWL® at 1 % concentration by weight. Then, Kolliphor ELP® (also called Cremophor ELP®) was added, and the mixture was homogenized under magnetic stirring at 37 °C for 10 min up to complete homogenization. To obtain 30-nm LNDs, the amounts of LabrafacWL® and Kolliphor ELP® were 40 and 60 mg, respectively, whereas for 80-nm LNDs, they were 57 and 43 mg, respectively. Finally, LNDs were generated with the addition of Milli-Q water (230 mg). Hydrodynamic diameter was measured by DLS using a Zetasizer Nano ZSP (Malvern Instruments S.A., Worcestershire, UK), using volume statistics. Absorption spectra were recorded on a Cary-5000 scan UV-visible spectrophotometer (Agilent, Santa Clara, CA,US), while emission spectra were recorded with a Spectrofluorometer FS5 (Edinburgh Instruments, Kirkton Campus, UK). The fluorescence spectra were corrected for detector response and lamp fluctuations. Fluorescence quantum yields of LNDs were measured using Rhodamine 101 in methanol as a reference (QY = 1.0) at excitation wavelength 530 nm (61).

Cranial window

The acute cranial window was prepared as described previously (11). Briefly, 7-8-week old C57/Bl6N mice obtained from Charles River Laboratories (Kisslegg, Germany) were anesthetized intraperitoneally (ip) with a solution containing medetomidine (0.5 mg/kg), fentanyl (0.05 mg/kg), and midazolam (5mg/kg) (MMF). Throughout the experiment, animals were endotracheally intubated and ventilated in a volume-controlled mode (MiniVent 845, Hugo Sachs Elektronik, March-Hungstetten, Germany); body temperature was monitored and maintained by a rectal probe attached to a feedback-controlled heating pad. In prone position, a rectangular 4×4-mm craniotomy was performed at the right fronto-parietal cortex under continuous cooling with saline. After removal of the bone flap and the dura mater, an exact fitting rectangular 4×4-mm cover glass of 0.175 μm thickness was placed upon the window and fixed onto the skull with dental cement.

Injection

For injection of LNDs and fluorescent vessel tracers we used an established femoral arterial catheterization protocol (11). 7.5 μL/g animal LnDs diluted 1:25 were injected for intravital imaging and 4 μL/g for the CCI study. Dextran, Cascade Blue™, 10000 Da MW (Thermo Fisher Scientific, Waltham, Massachusetts, US) was injected to define the BBB damaged area and Fluoresceinisothiocyanat-Dextran 0.5 %, 2000000 MW (Merk, Darmstatd, Germany) was injected to visualize the blood vessels *in vivo*, both in a dose of 3μL/g per mouse. DyLight 649 Labeled Lycopersicon Esculentum (Tomato) Lectin (Vector Laboratories, Burlingame, CA, US) 1 mg/ml for labelling of blood vessels was injected in a quantity of 0.1 ml per mouse. 30 nm gold nanoparticles with density 1.00 g/cm^3, methyl terminated, PEG 2000 coated (Sigma-Aldrich, St. Louis, Missouri, USA) were injected through femoral catheter into mouse in same dose as LNDs (7.5 μL/g animal).

2 photon image acquisition.

2-photon images were scanned as previously described (11). Briefly, the anesthetized mouse with cranial window was placed under an upright Zeiss LSM710 (Zeiss, Oberkochen, Germany) microscope and, after injection of FITC-dextran and localizing the region of interest (ROI) that represents most sizes and types of cerebral vessels, the baseline image was scanned. Next, immediately following injection of LnDs (30 nm or 80 nm), serial images were taken for 120 min. Ti:Sa laser (Chameleon Vision II) from 917 Coherent (Glasgow, Scotland) with an excitation wavelength of 830 nm and power of 5-22 % was used for detection. GAASP detector with an LP < 570 nm filter with master gain 600 for the FITC channel and LP > 570 nm for the LnDs (rhodamine) channel with master gain 560 were used. Images were taken as *z*-stacks (250 μm, 512 x 512, 8 bit, objective: W Plan-Apochromat 20x/1.0 DIC D=0.17 M27 75mm).

3D analysis of LnDs real-time circulation

Every acquired z-stack of intravital 2 photon imaging was processed through the Fiji macro, TubeAnalyst (IRB Barcelona) (28). First, using this algorithm, we identified and segmented vessels from z-stack, obtaining the total vessel volume and vessel mask. Next, we applied a generated mask on the non-processed z-stack, which allowed us to exclude the background and keep 3D fluorescence signal **(Figure 2C)**. Finally, using Fiji, we, calculated the total 3D fluorescence signal (Integrated Density) which, subsequently, was divided on total vessel volume, giving us fluorescence intensity per 1mm^3 of blood. Furthermore, in order to exclude fluctuations between animals and bleeding-through of FITC fluorescence, we normalized the obtained values to baseline and FITC.

Controlled Cortical Impact model of traumatic brain injury

Animals were subjected to experimental traumatic brain injury, using the previously described Controlled Cortical Impact (CCI) method (30, 62). This model induces a highly reproducible lesion that shares many characteristics of human TBI. In short, after induction of anesthesia with buprenorphine (100 mg/kg Bw) and isoflurane (4%, 30s), animals were sedated with 1,5-2,5% isoflurane in oxygen/ air under continuous monitoring of body temperature and heart rate. After right parietal craniotomy, the impact is directly applied to the intact dura with a pressure-controlled custom made CCI device (L. Kopacz, University of Mainz, Germany; 6 m/s, 0.5 mm penetration depth, 150 m contact time). For sham-surgery, the CCI device tip is placed on the dura after craniotomy, but no impact is induced. After re-fixation of the skull plate and surgical closure, animals are ventilated with 100% oxygen until the regained consciousness, then were kept in an incubator at 34°C and 60% humidity in order to prevent hypothermia. Stab injury was performed using a stereotactic frame as described previously (11).

Experiment design

All animal experiments were approved by Ethical Review Board of the Government of Upper Bavaria. The data were collected in accordance with the ARRIVE guidelines (63). Animal husbandry, health screens, and hygiene management checks were performed in accordance with Federation of European Laboratory Animal Science Associations (FELASA) guidelines and recommendations (64). 12 C57Bl/6N male mice, 23-25 g, underwent CCI as described above. 60 min post-CCI, mice were injected with 30 nm or 80 nm LnD (n=6). Animals were divided into early (30 min) and late (120 min) post-injection groups. In early group, LnDs injection was followed by Cascade Blue dextran (10,000 Da) injection, a very small and leaky dextran molecule that stains the injured area with opened BBB. In both groups, 5 minutes before sacrificing, animals received DyLight 649 Lectin to visualise perfused cerebral vessels. Animals were transcardially perfused with 4% PFA in deep anesthesia for immunohistochemical staining and with 2.5% of glutaraldehyde for correlative light-electron microscopy. For gold NPs and LNDs co-injection study, mouse (n=1) was sacrificed 60-min post-injection. For all groups, the lesion area of fixed brains was subsequently cut in vibratome in rostral-caudal direction into 50 µm sections as previously described (65). Afterwards, three selected sections were immediately mounted by Fluoromount™ (Sigma, St. Luis, MO, US), covered by cover slip (Menzel Gläser, Braunschweig, Germany) and directly scanned under confocal microscope.

Confocal image acquisition

Imaging was performed using confocal microscopy (ZEISS LSM 900, Carl Zeiss Microscopy GmbH, Jena Germany). For quantification of VO density, 10x magnification (EC Plan-Neofluar 10x/0.30 M27) was used with an image matrix of 1024 x 1024 pixel, a pixel scaling of 0.2 × 0.2 µm and a depth of 8 bit. Whole brain images were collected in z-stacks as tile scans with a slice-distance of 5 µm and a total range of 50 µm. For detailed analysis of extravasation, images were acquired with 40x magnification (EC Plan-Neofluar 40x/1.30 Oil DIC M27) with an image matrix of 1024 × 1024 pixel, a pixel scaling of 0.2 × 0.2 µm and a depth of 8 bit. For CLEM 3x3 tile z-stacks were acquired with 25x magnification (LD LCI Plan-Apochromat 25x/0.8 Imm Korr DIC M27) and image matrix 1024 × 1024 pixel, a pixel scaling of 0.2 × 0.2 µm and a depth of 8 bit. Specific regions of interest including the lesion site were collected in single plane.

Occlusion analysis. The occlusion density was analyzed in the area of co-localization of perfused vessels visualized by Lectin 649 and extravasated Cascade Blue (see above at Injection and Experimental Design). The size in mm^2 of this area was calculated at 3 coronal sections of each animal (n=3, per group) using Fiji. Inside the area, the number of occlusions with accumulated nanoparticles was calculated per mm^2. Statistical analysis performed using GraphPrism®, unpaired t-test. The vascular occlusions with accumulated NPs, where the fluorescent signal from rhodamine expanded over the border of the vessel (Lectin), was considered as VO with extravasation. The number of such VO was calculated *versus* the number of VO without extravasation at 3 coronal sections of each animal (n=3, per group) using Fiji. Statistical analysis performed using GraphPrism®, unpaired t-test.

Extravasation depth. The border between perfused and non-perfused areas was drawn based on labelling by DyLight 649 Lectin. The length of the border was measured using Fiji and assigned as a perimeter of the lesion. The area of extravasation at the outer part of the perimeter was measured using Fiji and, subsequently divided on the length of the perimeter. The obtained value was assigned as a depth of extravasation into the non-injured tissue. The intensity of extravasation was computed as a mean grey value using Fiji. The depth and intensity of extravasation was calculated at 3 coronal sections of each animal (n=3, per group). Statistical analysis performed using GraphPrism®, unpaired t-test.

Accumulation of LnDs in VO. The fluorescent intensity from the VO was calculated as a mean grey value using Fiji. The VOs from 3 coronal sections of each animal (n=3, per group) was analyzed, in total 146 occlusions in 30nm group and 341 – in 80 nm. Statistical analysis performed using GraphPrism®, unpaired t-test.

Correlative immunohistochemistry

Coronal brain sections were prepared using vibratome (Leica, Wetzlar, Germany) as described above. Since the lectin and LnDs were injected before perfusion of the mouse, no additional tissue processing was required. The lesion and peri-lesional area were scanned in confocal microscope in order to obtain non-affected signal from LnDs and vasculature. Afterwards, the sections were washed, blocked and simultaneously stained with the primary antibody in buffer (1% bovine serum albumin, 0.1% gelatin from cold water fish skin, 0.5% Triton X-100 in 0.01 M PBS, pH 7.2–7.4) for 72h at 4°C. The following primary antibodies were used: iba-1 (rabbit, Wako, #019-19741, 1:200), Ter119 (rat, Abcam, #ab91113, 1:100). After incubation, sections were washed in PBS and incubated with the following secondary antibodies: anti-rabbit coupled to Alexa Fluor® 488 (goat anti-rabbit, Thermo Fisher Scientific, #A-11073, 1:200), anti-rat coupled to Alexa Fluor® 594 (goat anti-guinea pig, Thermo Fisher Scientific, # A-11012, 1:200) in secondary antibody buffer (0.05% Tween 20 in 0.01 M PBS, pH 7.2–7.4). Nuclei were stained with 4′,6-Diamidin-2-phenylindol (DAPI, Invitrogen, #D1306) 1:10,000 in 0.01 M PBS. For caveolar staining conjugated Alexa Fluor® 488 Anti-Caveolin-1 antibody was used (rabbit, Abcam, # ab185043, 1:50). Then the same tissue sections were scanned again and vasculature patterns were used as tissue landmarks in order to match VO of interest with Iba-1, Ter119 or Cav-1 staining.

Microglia morphological analysis. To assess microglia morphology, maximum intensity projection of iba-1 stained sections were used. Microglia for quantification were selected according to their proximity to VOs. Using vascular landmarks for orientation, ROIs containing VOs were selected in the pre-stained sections and later superimposed onto the same section stained with iba-1 to identify the neighboring microglia cells. A total of 11-16 cells per section and group were selected.

Fractal analysis was performed to indicate circularity and directionality using a modified protocol from Young and Morrison (66). Z-stack images were converted to a maximum intensity projection and cells were individually cut out using the polygon selection tool in ImageJ. Only cells which were entirely contained within the z-stack were selected. Images were then thresholded and binarized as well as resized to 600 x 600 pixels, keeping the original scale. Any speckles and debris around the cell were removed using the paintbrush tool. After converting binary images to outlines, fractal analysis was performed using the FracLac plugin for ImageJ (67). As described previously (66), the total number of pixels present in the cell image of either the filled or outlined binary image were calculated and later transformed to µm2 (pixel area = 0,208 µm2). Cell circularity was calculated as

$$\text{Circularity} = 4*\pi*\text{Area}/\text{Perimeter}^2.$$

Directionality of the cell was assessed by using the maximum and minimum span ratio across the convex hull (68).

Cell culture experiments.

Mixed cortical cell culture. Primary mixed cortical cultures were prepared from cortices of E17 embryonic Sprague-Dawley rat pups (Charles-River, kindly provided by Sabina Tahirovic) as previously described (11). In short, cortices were treated with DNaseI (10 µg/mL, Roche), triturated and plated on round glass coverslips (~275 cells/mm2) coated with poly-D-lysine (0.1 mg/mL). Cells were plated in Neurobasal-A medium supplemented with 2% B-27, 2 mM GlutaMAX and 100 U/mL penicillin-streptomycin, containing 10 mM glucose and 1 mM pyruvate. Half of the media was exchanged after 6-24 h and subsequently two times every week. Cells were cultured to maturity for 21 days in cell culture incubators at 37°C and 5% CO2/95% air).

Nanoparticle uptake assay. To assess neuronal uptake of nanoparticles, we added 10 µL of nanoparticles into each well at different time points and incubated them with cells for total incubation times of 30 min, 60 min, 90 min and 120 min respectively. After incubation, cells were washed 3 times with 1x PBS and fixed for 15 min with 3.7% PFA/sucrose in PBS. Cells were washed 3 times with PBS and incubated for 10 min with 50 mM NH4Cl to quench free aldehyde groups. After 3 further washes with PBS, cells were stored in PBS at 4°C until staining.

Immunofluorescence staining. Fixed mixed cortical cultures were blocked at RT for 1 h with a blocking buffer containing 0.2% BSA, 0.2% FBS and 0.02% fish gelatin in PBS. Staining was performed by incubating cells with 1:1000 anti-β-Tubulin-III (mouse, T8578, Sigma) in blocking buffer for 3 h at RT. After 3 washes with PBS, anti-mouse coupled to Alexa Fluor 488 (donkey anti-mouse, 1:1000, 0.75 mg/mL, 715-546-150, Jackson Immuno Research) was incubated for 30 min. Nuclei were stained with 1:5000 DAPI for 5 min before final washes and mounting.

Confocal image acquisition. Imaging was performed using confocal microscopy (ZEISS LSM 900, Carl Zeiss Microscopy GmbH, Jena Germany). 3x3 tile z-stacks were acquired with 25x magnification (LD LCI Plan-Apochromat 25x/0.8 Imm Korr DIC M27) and image matrix 1024 × 1024 pixel, a pixel scaling of 0.2 × 0.2 µm and a depth of 8 bit.

Correlated light and ATUM Volume Scanning Electron Microscopy (CLEM).

Mice were perfused in fixative (4% PFA and 2.5% glutaraldehyde in 0.1 M sodium cacodylate buffer, pH 7.4; Science Services) and brains immersion fixed for 24h, vibratome sectioned coronally and incubated for another 24h in the same fixative and stored in PBS.

Confocal – mounting, imaging conditions, demounting. The sections were stored in PBS at 4°C until the start of the postembedding. The cortical region of interest (roughly 1.5 x 1.5 mm) was identified by comparison with the confocal overview scan and trimmed under a dissecting microscope using fine scalpels. We applied a standard rOTO en bloc staining protocol (33) including postfixation in 2% osmium tetroxide (EMS), 1.5% potassium ferricyanide (Sigma) in 0.1 M sodium cacodylate (Science Services) buffer (pH 7.4). Staining was enhanced by reaction with 1% thiocarbohydrazide (Sigma) for 45 min at 40°C. The tissue was washed in water and incubated in 2% aqueous osmium tetroxide, washed and further contrasted by overnight incubation in 1% aqueous uranyl acetate at 4°C and 2h at 50°C. Samples were dehydrated in an ascending ethanol series and infiltrated with LX112 (LADD).

For the volume analysis, the block was trimmed by 200 µm at a 90° angle on each side using a TRIM90 diamond knife (Diatome) on the ATUMtome (Powertome, RMC). Serial sections were taken with a 35° ultra-maxi diamond knife (Diatome) at a nominal cutting thickness of 100 nm and collected on freshly plasma-treated (custom-built, based on Pelco easiGlow, adopted from M. Terasaki, U. Connecticut, CT), carbon nanotube (CNT) tape (Science Services). Covering the whole sample thickness of 80 µm and considering its unevenness after contrasting, 1000 sections were taken.

CNT tape stripes were assembled onto adhesive carbon tape (Science Services) attached to 4-inch silicon wafers (Siegert Wafer) and grounded by adhesive carbon tape strips (Science Services). EM micrographs were acquired on a Crossbeam Gemini 340 SEM (Zeiss) with a four-quadrant backscatter detector at 8 kV. In ATLAS5 Array Tomography (Fibics), wafer overview images were generated (1000 nm/pixel).

We acquired whole section low (0.5 x 0.5 x 2 µm) and medium resolution (0.1 x 0.1 x 2 µm) volumes of the area of interest (550 x 630 x 60 μm^3) to facilitate relocation. Anatomical landmarks and vasculature patterns of single and summed sections were compared to the confocal data sets in Fiji (69). Within this volume clots were selected for high resolution imaging (clot C: 4 x 4 x 200 nm, 70 x 95 x 70 µm; clotA: 20 x 20 x 200 nm, 270 x 190 x 26 µm). Serial section data were aligned by a sequence of automated and manual processing steps in Fiji TrakEM2 (69). VAST software was used for manual segmentation (70) and Blender for rendering and movie generation (71) of luminal and extraluminal structures of the neurovascular unit.

Statistical Analysis. Statistical analysis was performed using GraphPrism® software. Data are presented as mean ± standard deviation. For real-time brightness of NPs, unpaired t-test was used (n=6 mice); for circulation kinetics, two-way ANOVA with post-hoc Tukey correction for multiple comparison was used (n=6 mice). For density of occlusions and extravasations in the TBI brain, unpaired t-test was used (3 mice, 9 sections). For depth of particles penetration in penumbra, unpaired t-test was used (3 mice, 9 sections, 15 regions of interest). For the number of accumulated NPs inside VOs, unpaired t-test was used (3 mice, 9 sections, 146 and 341 clots). For morphological analysis of microglia (circularity and directionality), unpaired t-test was used (n=15 cells).

ACKNOWLEDGEMENTS

We thank Georg Kislinger and Hanyi Jiang for segmentation and rendering of the 3D EM model. This work was supported by the European Union Horizon 2020 research and innovation program under the Marie Skłodowska-Curie grant agreement No 794094, the European Research Council ERC Consolidator grant BrightSens 648528, the Agence National de Recherche JC/JC grant “Supertrack” ANR-16-CE09-0007, funded by the Deutsche Forschungsgemeinschaft (DFG, German Research Foundation) – projects number: 457586042, FOR2879; A03 – Mi 694/9-1 - 428663564; DFG under Germany’s Excellence Strategy within the framework of the Munich Cluster for Systems Neurology (EXC 2145 SyNergy—ID 390857198) and the TRR 274/1 2020 – 408885537 (project Z01).

REFERENCES:

1. Wilson L, Horton L, Kunzmann K, Sahakian BJ, Newcombe VF, Stamatakis EA, et al. Understanding the relationship between cognitive performance and function in daily life after traumatic brain injury. 2021;92(4):407-17.

2. Smith DH, Johnson VE, Stewart W. Chronic neuropathologies of single and repetitive TBI: substrates of dementia? Nat Rev Neurol. 2013;9(4):211-21.

3. Kabadi SV, Faden AI. Neuroprotective strategies for traumatic brain injury: improving clinical translation. Int J Mol Sci. 2014;15(1):1216-36.

4. Alyautdin R, Khalin I, Nafeeza MI, Haron MH, Kuznetsov D. Nanoscale drug delivery systems and the blood-brain barrier. International journal of nanomedicine. 2014;9:795-811.

5. Mitchell MJ, Billingsley MM, Haley RM, Wechsler ME, Peppas NA, Langer R. Engineering precision nanoparticles for drug delivery. Nature Reviews Drug Discovery. 2021;20(2):101-24.

6. Li W, Qiu J, Li X-L, Aday S, Zhang J, Conley G, et al. BBB pathophysiology–independent delivery of siRNA in traumatic brain injury. 2021;7(1):eabd6889.

7. Cruz LJ, Stammes MA, Que I, van Beek ER, Knol-Blankevoort VT, Snoeks TJA, et al. Effect of PLGA NP size on efficiency to target traumatic brain injury. Journal of controlled release : official journal of the Controlled Release Society. 2016;223:31-41.

8. Kwon EJ, Skalak M, Lo Bu R, Bhatia SN. Neuron-Targeted Nanoparticle for siRNA Delivery to Traumatic Brain Injuries. ACS Nano. 2016;10(8):7926-33.

9. Yoo D, Magsam AW, Kelly AM, Stayton PS, Kievit FM, Convertine AJ. Core-Cross-Linked Nanoparticles Reduce Neuroinflammation and Improve Outcome in a Mouse Model of Traumatic Brain Injury. ACS Nano. 2017;11(9):8600-11.

10. Khalin I, Alyautdin R, Wong TW, Gnanou J, Kocherga G, Kreuter J. Brain-derived neurotrophic factor delivered to the brain using poly (lactide-co-glycolide) nanoparticles improves neurological and cognitive outcome in mice with traumatic brain injury. Drug delivery. 2016;23(9):3520-8.

11. Khalin I, Heimburger D, Melnychuk N, Collot M, Groschup B, Hellal F, et al. Ultrabright Fluorescent Polymeric Nanoparticles with a Stealth Pluronic Shell for Live Tracking in the Mouse Brain. ACS Nano. 2020;14(8):9755-70.

12. Henrich-Noack P, Nikitovic D, Neagu M, Docea AO, Engin AB, Gelperina S, et al. The blood-brain barrier and beyond: Nano-based neuropharmacology and the role of extracellular matrix. Nanomedicine : nanotechnology, biology, and medicine. 2019;17:359-79.

13. Israel LL, Galstyan A, Holler E, Ljubimova JY. Magnetic iron oxide nanoparticles for imaging, targeting and treatment of primary and metastatic tumors of the brain. Journal of Controlled Release. 2020;320:45-62.

14. Kreuter J. Drug delivery to the central nervous system by polymeric nanoparticles: what do we know? Advanced drug delivery reviews. 2014;71:2-14.

15. Vogel AB, Kanevsky I, Che Y, Swanson KA, Muik A, Vormehr M, et al. BNT162b vaccines protect rhesus macaques from SARS-CoV-2. Nature. 2021;592(7853):283-9.

16. Teleanu DM, Chircov C, Grumezescu AM, Teleanu RI. Neuronanomedicine: An Up-to-Date Overview. Pharmaceutics. 2019;11(3):101.

17. Anton N, Benoit JP, Saulnier P. Design and production of nanoparticles formulated from nano-emulsion templates-a review. Journal of controlled release : official journal of the Controlled Release Society. 2008;128(3):185-99.

18. Klymchenko AS, Liu F, Collot M, Anton N. Dye-Loaded Nanoemulsions: Biomimetic Fluorescent Nanocarriers for Bioimaging and Nanomedicine. Advanced healthcare materials. 2021;10(1):e2001289.

19. Marschallinger J, Iram T, Zardeneta M, Lee SE, Lehallier B, Haney MS, et al. Lipid-droplet-accumulating microglia represent a dysfunctional and proinflammatory state in the aging brain. Nature Neuroscience. 2020;23(2):194-208.

20. Bouchaala R, Mercier L, Andreiuk B, Mély Y, Vandamme T, Anton N, et al. Integrity of lipid nanocarriers in bloodstream and tumor quantified by near-infrared ratiometric FRET imaging in living mice. Journal of controlled release : official journal of the Controlled Release Society. 2016;236:57-67.

21. Kilin VN, Anton H, Anton N, Steed E, Vermot J, Vandamme TF, et al. Counterion-enhanced cyanine dye loading into lipid nano-droplets for single-particle tracking in zebrafish. Biomaterials. 2014;35(18):4950-7.

22. Khalin I, Severi C, Heimburger D, Wehn A, Hellal F, Reisch A, et al. Dynamic tracing using ultra-bright labeling and multi-photon microscopy identifies endothelial uptake of poloxamer 188 coated poly(lactic-co-glycolic acid) nano-carriers in vivo. Nanomedicine: Nanotechnology, Biology and Medicine. 2022;40:102511.

23. Reisch A, Didier P, Richert L, Oncul S, Arntz Y, Mély Y, et al. Collective fluorescence switching of counterion-assembled dyes in polymer nanoparticles. Nature Communications. 2014;5(1):4089.

24. Reisch A, Runser A, Arntz Y, Mély Y, Klymchenko AS. Charge-Controlled Nanoprecipitation as a Modular Approach to Ultrasmall Polymer Nanocarriers: Making Bright and Stable Nanoparticles. ACS Nano. 2015;9(5):5104-16.

25. Anton N, Vandamme TF. Nano-emulsions and micro-emulsions: clarifications of the critical differences. Pharmaceutical research. 2011;28(5):978-85.

26. Xu C, Webb WW. Measurement of two-photon excitation cross sections of molecular fluorophores with data from 690 to 1050 nm. J Opt Soc Am B. 1996;13(3):481-91.

27. Andreiuk B, Reisch A, Bernhardt E, Klymchenko AS. Fighting Aggregation-Caused Quenching and Leakage of Dyes in Fluorescent Polymer Nanoparticles: Universal Role of Counterion. 2019;14(6):836-46.

28. Jeon JS, Bersini S, Whisler JA, Chen MB, Dubini G, Charest JL, et al. Generation of 3D functional microvascular networks with human mesenchymal stem cells in microfluidic systems. Integr Biol (Camb). 2014;6(5):555-63.

29. Wehn AC, Khalin I, Duering M, Hellal F, Culmsee C, Vandenabeele P, et al. RIPK1 or RIPK3 deletion prevents progressive neuronal cell death and improves memory function after traumatic brain injury. Acta Neuropathologica Communications. 2021;9(1):138.

30. Schwarzmaier SM, Kim SW, Trabold R, Plesnila N. Temporal profile of thrombogenesis in the cerebral microcirculation after traumatic brain injury in mice. J Neurotrauma. 2010;27(1):121-30.

31. Wu H-M, Huang S-C, Vespa P, Hovda DA, Bergsneider M. Redefining the pericontusional penumbra following traumatic brain injury: evidence of deteriorating metabolic derangements based on positron emission tomography. J Neurotrauma. 2013;30(5):352-60.

32. Mastorakos P, Mihelson N, Luby M, Burks SR, Johnson K, Hsia AW, et al. Temporally distinct myeloid cell responses mediate damage and repair after cerebrovascular injury. Nature Neuroscience. 2021;24(2):245-58.

33. Kislinger G, Gnägi H, Kerschensteiner M, Simons M, Misgeld T, Schifferer M. ATUM-FIB microscopy for targeting and multiscale imaging of rare events in mouse cortex. STAR Protocols. 2020;1(3):100232.

34. Nowak M, Helgeson ME, Mitragotri S. Delivery of Nanoparticles and Macromolecules across the Blood–Brain Barrier. 2020;3(1):1900073.

35. Waggoner LE, Madias MI, Hurtado AA, Kwon EJ. Pharmacokinetic Analysis of Peptide-Modified Nanoparticles with Engineered Physicochemical Properties in a Mouse Model of Traumatic Brain Injury. The AAPS Journal. 2021;23(5):100.

36. Bharadwaj VN, Lifshitz J, Adelson PD, Kodibagkar VD, Stabenfeldt SE. Temporal assessment of nanoparticle accumulation after experimental brain injury: Effect of particle size. Scientific Reports. 2016;6(1):29988.

37. Munter R, Kristensen K, Pedersbaek D, Larsen JB, Simonsen JB, Andresen TL. Dissociation of fluorescently labeled lipids from liposomes in biological environments challenges the interpretation of uptake studies. Nanoscale. 2018;10(48):22720-4.

38. Reisch A, Didier P, Richert L, Oncul S, Arntz Y, Mely Y, et al. Collective fluorescence switching of counterion-assembled dyes in polymer nanoparticles. Nat Commun. 2014;5:4089.

39. Khalin I, Severi C, Heimburger D, Wehn A, Hellal F, Reisch A, et al. Highly fluorescent biodegradable PLGA nano-carriers allow real-time tracking of individual particles in vivo. 2020:2020.11.19.385062.

40. Zinger A, Soriano S, Baudo G, De Rosa E, Taraballi F, Villapol S. Biomimetic Nanoparticles as a Theranostic Tool for Traumatic Brain Injury. 2021;31(30):2100722.

41. Hoshyar N, Gray S, Han H, Bao G. The effect of nanoparticle size on in vivo pharmacokinetics and cellular interaction. Nanomedicine (Lond). 2016;11(6):673-92.

42. Stein SC, Graham DI, Chen XH, Smith DH. Association between intravascular microthrombosis and cerebral ischemia in traumatic brain injury. Neurosurgery. 2004;54(3):687-91; discussion 91.

43. Stein SC, Chen XH, Sinson GP, Smith DH. Intravascular coagulation: a major secondary insult in nonfatal traumatic brain injury. Journal of neurosurgery. 2002;97(6):1373-7.

44. Schwarzmaier SM, de Chaumont C, Balbi M, Terpolilli NA, Kleinschnitz C, Gruber A, et al. The Formation of Microthrombi in Parenchymal Microvessels after Traumatic Brain Injury Is Independent of Coagulation Factor XI. J Neurotrauma. 2016;33(17):1634-44.

45. Albert-Weissenberger C, Hopp S, Nieswandt B, Sirén A-L, Kleinschnitz C, Stetter C. How is the formation of microthrombi after traumatic brain injury linked to inflammation? Journal of Neuroimmunology. 2019;326:9-13.

46. Lu D, Mahmood A, Goussev A, Qu C, Zhang ZG, Chopp M. Delayed thrombosis after traumatic brain injury in rats. J Neurotrauma. 2004;21(12):1756-66.
47. Sandsmark DK, Bashir A, Wellington CL, Diaz-Arrastia R. Cerebral Microvascular Injury: A Potentially Treatable Endophenotype of Traumatic Brain Injury-Induced Neurodegeneration. Neuron. 2019;103(3):367-79.
48. Wu Y, Wu H, Guo X, Pluimer B, Zhao Z. Blood-Brain Barrier Dysfunction in Mild Traumatic Brain Injury: Evidence From Preclinical Murine Models. Front Physiol. 2020;11:1030-.
49. Schwarzmaier SM, Gallozzi M, Plesnila N. Identification of the Vascular Source of Vasogenic Brain Edema following Traumatic Brain Injury Using In Vivo 2-Photon Microscopy in Mice. J Neurotrauma. 2015;32(13):990-1000.
50. Zweckberger K, Plesnila N. Anatibant, a selective non-peptide bradykinin B2 receptor antagonist, reduces intracranial hypertension and histopathological damage after experimental traumatic brain injury. Neurosci Lett. 2009;454(2):115-7.
51. Plesnila N, Schulz J, Stoffel M, Eriskat J, Pruneau D, Baethmann A. Role of bradykinin B2 receptors in the formation of vasogenic brain edema in rats. J Neurotrauma. 2001;18(10):1049-58.
52. Krueger M, Bechmann I, Immig K, Reichenbach A, Härtig W, Michalski D. Blood-brain barrier breakdown involves four distinct stages of vascular damage in various models of experimental focal cerebral ischemia. Journal of cerebral blood flow and metabolism : official journal of the International Society of Cerebral Blood Flow and Metabolism. 2015;35(2):292-303.
53. Egloff S, Runser A, Klymchenko A, Reisch A. Size-Dependent Electroporation of Dye-Loaded Polymer Nanoparticles for Efficient and Safe Intracellular Delivery. 2021;5(2):2000947.
54. Ahrens ET, Bulte JW. Tracking immune cells in vivo using magnetic resonance imaging. Nature reviews Immunology. 2013;13(10):755-63.
55. Wang Z, Tiruppathi C, Minshall RD, Malik AB. Size and Dynamics of Caveolae Studied Using Nanoparticles in Living Endothelial Cells. ACS Nano. 2009;3(12):4110-6.
56. Predescu SA, Predescu DN, Malik AB. Molecular determinants of endothelial transcytosis and their role in endothelial permeability. American journal of physiology Lung cellular and molecular physiology. 2007;293(4):L823-42.
57. Kamali-Zare P, Nicholson C. Brain extracellular space: geometry, matrix and physiological importance. Basic Clin Neurosci. 2013;4(4):282-6.
58. Thorne RG, Nicholson C. In vivo diffusion analysis with quantum dots and dextrans predicts the width of brain extracellular space. Proceedings of the National Academy of Sciences of the United States of America. 2006;103(14):5567-72.
59. Chen YY, Syed AM, MacMillan P, Rocheleau JV, Chan WCW. Flow Rate Affects Nanoparticle Uptake into Endothelial Cells. 2020;32(24):1906274.
60. Boyd BJ, Galle A, Daglas M, Rosenfeld JV, Medcalf R. Traumatic brain injury opens blood-brain barrier to stealth liposomes via an enhanced permeability and retention (EPR)-like effect. Journal of drug targeting. 2015;23(9):847-53.
61. Karstens T, Kobs K. Rhodamine B and rhodamine 101 as reference substances for fluorescence quantum yield measurements. The Journal of Physical Chemistry. 1980;84(14):1871-2.
62. Chen S, Mao X, Lin X, Wehn A, Hu S, Mamrak U, et al. Acid-ion sensing channel 1a deletion reduces chronic brain damage and neurological deficits after experimental traumatic brain injury. J Neurotrauma. 2021.
63. Kilkenny C, Browne WJ, Cuthill IC, Emerson M, Altman DG. Improving bioscience research reporting: the ARRIVE guidelines for reporting animal research. PLoS Biol. 2010;8(6):e1000412.
64. Guillen J. FELASA guidelines and recommendations. J Am Assoc Lab Anim Sci. 2012;51(3):311-21.
65. Ghosh M, Balbi M, Hellal F, Dichgans M, Lindauer U, Plesnila N. Pericytes are involved in the pathogenesis of cerebral autosomal dominant arteriopathy with subcortical infarcts and leukoencephalopathy. Ann Neurol. 2015;78(6):887-900.
66. Young K, Morrison H. Quantifying Microglia Morphology from Photomicrographs of Immunohistochemistry Prepared Tissue Using ImageJ. J Vis Exp. 2018(136).

67. Karperien A. FracLac for ImageJ. 1999-2013.

68. Fernandez-Arjona MDM, Grondona JM, Granados-Duran P, Fernandez-Llebrez P, Lopez-Avalos MD. Microglia Morphological Categorization in a Rat Model of Neuroinflammation by Hierarchical Cluster and Principal Components Analysis. Front Cell Neurosci. 2017;11:235.

69. Schindelin J, Arganda-Carreras I, Frise E, Kaynig V, Longair M, Pietzsch T, et al. Fiji: an open-source platform for biological-image analysis. Nature methods. 2012;9(7):676-82.

70. Berger DR, Seung HS, Lichtman JW. VAST (Volume Annotation and Segmentation Tool): Efficient Manual and Semi-Automatic Labeling of Large 3D Image Stacks. Front Neural Circuits. 2018;12:88.

71. Brito A. Blender Quick Start Guide: 3D Modeling, Animation, and Render with Eevee in Blender 2.8: Packt Publishing; 2018.